



HAL
open science

Thinning mechanisms of heterogeneous continental lithosphere

Benoit Petri, Thibault Duretz, Geoffroy Mohn, Stefan M Schmalholz, Garry D. Karner, Othmar Müntener

► **To cite this version:**

Benoit Petri, Thibault Duretz, Geoffroy Mohn, Stefan M Schmalholz, Garry D. Karner, et al.. Thinning mechanisms of heterogeneous continental lithosphere. *Earth and Planetary Science Letters*, 2019, 512, pp.147-162. 10.1016/j.epsl.2019.02.007 . insu-02044661

HAL Id: insu-02044661

<https://insu.hal.science/insu-02044661>

Submitted on 6 Nov 2019

HAL is a multi-disciplinary open access archive for the deposit and dissemination of scientific research documents, whether they are published or not. The documents may come from teaching and research institutions in France or abroad, or from public or private research centers.

L'archive ouverte pluridisciplinaire **HAL**, est destinée au dépôt et à la diffusion de documents scientifiques de niveau recherche, publiés ou non, émanant des établissements d'enseignement et de recherche français ou étrangers, des laboratoires publics ou privés.

1 **Thinning mechanisms of heterogeneous continental lithosphere**

2

3 Benoît PETRI^{1*}, Thibault DURETZ^{1,2}, Geoffroy MOHN³, Stefan M. SCHMALHOLZ¹, Garry
4 D. KARNER⁴, Othmar MÜNTENER¹

5

6 ¹ *Institute of Earth Sciences, University of Lausanne, Géopolis, 1015 Lausanne, Switzerland*

7 ² *Univ Rennes, CNRS, Géosciences Rennes UMR 6118, F-35000 Rennes, France*

8 ³ *Département Géosciences et Environnement, Université de Cergy-Pontoise, 5, mail Gay
9 Lussac, Neuville-sur-Oise, 95031 Cergy-Pontoise Cedex, France*

10 ⁴ *ExxonMobil Exploration Company, 22777 Springwoods Village Pkwy, Spring, Houston, TX-
11 77389, USA*

12

13 *Corresponding author: bpetri@unistra.fr

14

15 ORCID Petri: 0000-0001-7142-0406

16 ORCID Duretz: 0000-0001-8472-7490

17 ORCID Mohn: 0000-0002-8729-2960

18 ORCID Schmalholz: 0000-0003-4724-2181

19 ORCID Müntener: 0000-0002-7771-4381

20 ORCID Karner: /

21 **HIGHLIGHTS**

- 22 • Pre-rift architecture of the continental lithosphere is important during rifting
- 23 • Initial mechanical heterogeneities control strain partitioning
- 24 • Extraction tectonics is an efficient thinning mechanism
- 25 • Various crustal levels can be exhumed in distal margins

26 **KEYWORDS**

- 27 • Rifting
- 28 • Rifted margin
- 29 • Lithospheric thinning
- 30 • Extraction tectonics
- 31 • Inheritance

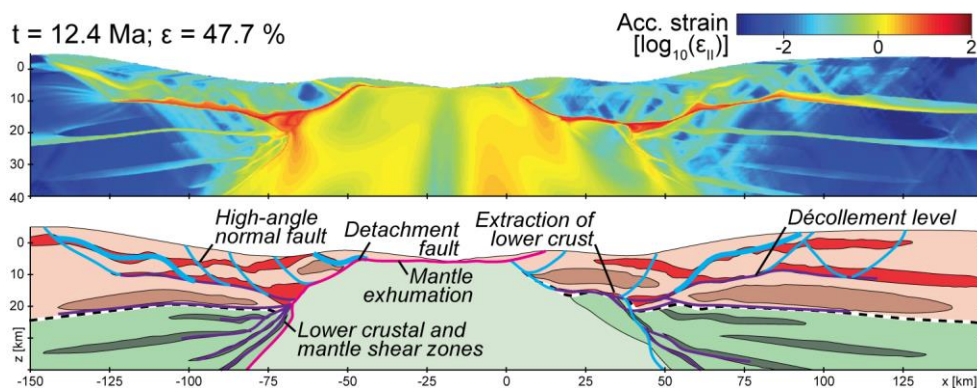
32 **ABSTRACT**

33 The mechanisms responsible for the formation of extremely thinned continental crust
34 (< 10 km thick) and lithosphere during rifting remains debated. Observations from present-
35 day and fossil passive margins highlight the role of deep-seated deformation, likely controlled
36 by heterogeneities within the continental lithosphere, such as changing lithologies,
37 mechanical anisotropies and inherited structures. We investigate the mechanisms of
38 lithospheric thinning by exploring the role of pre-existing heterogeneities on the architecture
39 and evolution of rifted margins. We estimate pre-rift pressure conditions (P_0) vs. depth
40 diagrams of crustal to lithospheric sections, to quantify rift-related modifications on inherited
41 lithostatic pressure gradients. Two field examples from the Alpine Tethys margins in the
42 Eastern and Southern Alps (SE Switzerland and N Italy) were selected to characterize: (1) the
43 pre-rift architecture of the continental lithosphere; (2) the localization of rift-related
44 deformation in distinct portions of the lithosphere; and (3) the interaction between pre-

45 existing heterogeneities of the lithosphere and rift-related structures. These observations are
46 compared with high-resolution, two-dimensional thermo-mechanical numerical models. The
47 design of the models takes into account pre-existing mechanical heterogeneities representing
48 the initial pre-rift architecture of the continental lithosphere. Extensional structures consist of
49 high-angle and low-angle normal faults, anastomosing shear-zones and decoupling horizons.
50 Such structures accommodate the lateral extraction of mechanically stronger levels derived
51 from the middle to lower crust. As a result, the extremely thinned continental crust in Tethyan
52 passive margins represents the juxtaposition and amalgamation of distinct strong levels of the
53 crust separated by major extensional structures identified by sharp pressure gradients. Future
54 work should determine the applicability of these results to other present-day and fossil rifted
55 margins.

56 GRAPHICAL ABSTRACT

57



58 **1. INTRODUCTION**

59 The increased number of high-quality geophysical surveys across continental rifted
60 margins has allowed to recognize the characteristic first-order architecture of margins.
61 Commonly, rifted margins that approach break-up are the result of extreme crustal and
62 lithospheric thinning. The crustal thickness typically passes from 30-35 km to less than 10 km
63 over a distance of a hundred kilometers (e.g. Osmundsen and Ebbing, 2008). Reflection
64 seismic data indicate that the deformation of upper crustal levels is achieved through high-
65 angle and low-angle normal faulting (e.g. Whitmarsh et al., 2000), but attempts to restore
66 displacements accommodated along these brittle, upper-crustal extensional structures fail in
67 explaining the observed amount of lithospheric thinning (e.g., Kusznir and Karner, 2007;
68 Reston, 2007a). Deep, intra-basement deformation likely plays a critical role in such extreme
69 crustal and lithospheric thinning (Huisman and Beaumont, 2014; Karner et al., 2003). The
70 direct characterization of this deeper deformation remains elusive in present-day rifted
71 margins and has only been described for a small number of margins (Clerc et al., 2018, 2015;
72 Reston, 1988). In contrast, many conceptual models have been proposed for a wide range of
73 deformation styles involving, among others, oceanward or continentward lower crustal “flow”
74 and crustal necking (Reston, 2007b).

75 Indeed, contrary to the upper crustal deformation, the localization, partitioning, and
76 deformation style of extensional structures at depth may be controlled by the lithological,
77 structural and thermal state of the continental lithosphere (e.g. Duretz et al., 2016b). The
78 spatial and temporal heterogeneity of the lithosphere, having various petrological, chemical,
79 mechanical and thermal characteristics, has been noted in some places (Rader et al., 2015;
80 Thybo and Artemieva, 2013) as well as its impact on the architecture and evolution of rifted
81 margins (e.g. Tommasi and Vauchez, 2001; Zastrozhnov et al., 2018). However, their detailed

82 role and influence on the mechanisms of crustal and lithospheric stretching and thinning
83 remain elusive.

84 The objective of this contribution is to investigate the mechanisms of extreme
85 lithospheric thinning by exploring the role of initial or pre-existing mechanical heterogeneities
86 on the architecture and evolution of passive margins by comparing field-derived observations
87 and quantification to numerical models. In contrast to present-day rifted margins, deep
88 extensional, exposed rift-related structures have been mapped and can be accessed in fossil
89 equivalents preserved in present-day orogens. Field observations from the Alps in Western
90 Europe preserving the Alpine Tethys remnants enable us to characterize and describe the first-
91 order relations between rift-related structures and the initial heterogeneities of the continental
92 lithosphere. These observations are subsequently incorporated into high-resolution, two-
93 dimensional thermo-mechanical numerical models of lithospheric extensional deformation.

94 **2. APPROACH**

95 The characterization of rift-related, intra-basement deformation relies on being able to
96 sample rocks of the extended continental lithosphere. In particular, exposure of distinct
97 portions of the continental lithosphere is possible when rifted margins have been thrust and
98 uplifted in orogens (Beltrando et al., 2014; Dewey and Bird, 1970). There, under certain
99 conditions, the pre-, syn- and post-rift history can be determined (Beltrando et al., 2013;
100 Frasca et al., 2016; Mohn et al., 2010) from both the stratigraphic and basement evolution
101 (Fig. 1). However, investigating the role of initial heterogeneities during rifting requires key
102 prerequisites: (1) recognition of rift-related structures from pre- and post-rift (i.e. orogenic,
103 post-orogenic) structures; and (2) detailed pressure – temperature – time – deformation (*P-T-*
104 *t-d*) evolution of distinct portions of the continental lithosphere.

105 The Alps, preserving the remnants of the Alpine Tethys margins, satisfy these
106 requirements. More than a century of research in these areas permits the recognition of rift

107 structures related to the opening of the Alpine Tethys and its evolution (see Mohn et al., 2010
108 for a review). Here, we focus on the remnants of the Alpine Tethys preserved in the Eastern
109 Alps (SE Switzerland and N Italy, Fig. 2ab) and in the Southern Alps (N Italy, Fig. 2ac).
110 These portions of the fossil Adriatic margin have been reactivated and incorporated into the
111 Alpine orogen during the Cretaceous to Oligocene/Miocene but escaping significant Alpine
112 deformation and metamorphic overprint (Fig. 2bc; see Mohn et al., 2011 for the Central Alps;
113 Schmid et al., 1987; Wolff et al., 2012 for the Southern Alps).

114 The Paleozoic basement sampled in both the Eastern and Southern Alps records a
115 protracted, polyphase tectonic history. After crustal amalgamation and accretion during the
116 Devonian and Carboniferous Variscan phases (von Raumer et al., 2013), the continental
117 lithosphere underwent a major reorganization during the late Carboniferous and early Permian
118 (e.g. Petri et al., 2017) during which the continental crust returned back to an equilibrated
119 thickness (30-35 km). Extensional tectonics, together with mantle-derived magmatic under-
120 and intra-plating, caused differentiation of the continental crust with granulite, amphibolite
121 and greenschist facies rocks in the lower, middle and upper crust, respectively (Schuster and
122 Stüwe, 2008). Although diffuse and low-magnitude Triassic rifting is locally documented
123 (e.g. Bertotti et al., 1993), no evidence for major exhumation and thinning of the continental
124 lithosphere from the Permian post-orogenic event until the Jurassic rifting has been described.
125 This conclusion is based on two key arguments: (1) isobaric cooling was reported for Permian
126 magmatism and associated contact metamorphism (Müntener et al., 2000; Petri et al., 2016);
127 and (2) the Triassic stratigraphic record, consisting of fluvial to shallow-marine deposits,
128 precludes any major crustal thinning during this time. Therefore, we consider the late
129 Carboniferous and early Permian magmatic intrusions and associated metamorphism as points
130 of reference in terms of their exhumation history during Jurassic rifting.

131 The depth of these magmatic intrusions, and the associated contact metamorphism,
132 have been determined by many studies across the Alps (see Spalla et al., 2014 for a review).
133 Such datasets provide approximate pre-rift pressure conditions (P_0) for the magmatic and
134 metamorphic rocks prior to Jurassic exhumation. Using an average continental crust density
135 ($2.7\text{-}3.0\text{ g.cm}^{-3}$; Fountain and Salisbury, 1981), the pre-rift architecture of the Alpine
136 basement can be locally reconstructed (A-A' on Fig. 1b) and rift-related pressure effects in the
137 crust can be tracked: in a pre-rift section, data are aligned along an average lithostatic gradient
138 ($0.26\text{-}0.29\text{ kbar.km}^{-1}$) while rift-related extension modifies the inherited P_0 -depth gradients
139 generating either jumps in P_0 with depth (sharp gradient, e.g., missing middle crust) or an
140 increased gradient if deformation is “homogeneously” distributed during thinning (e.g.
141 “ductile flow”; B-B' on Fig. 1b). Such information on pressure gradients can be extracted
142 from both field observations and numerical models. These approaches will be applied to two
143 sections across the reconstructed Jurassic Adriatic rift margin from the proximal to the distal
144 domains. The field observations and associated P_0 -depth gradients (see Tables S1 and S2 for
145 full P_0 dataset) will be compared with results of numerical simulations in order to propose a
146 model for the evolution and mechanisms of continental lithosphere thinning of the Alpine
147 Tethys rifted margins.

148 **3. THE EASTERN ALPS CASE STUDY**

149 The Eastern Alps preserved the remnants of the Adriatic rifted margin that has been
150 variably reactivated during the Alpine orogeny from Late Cretaceous to Tertiary (Figs. 2ab-4;
151 Froitzheim et al., 1994; Mohn et al., 2011). Two distinct Alpine nappe stacks have been
152 identified and are separated by the Lunghin-Mortirolo Movement Zone (LMMZ). To the
153 north, the Err - Platta and Campo - Grosina nappe stacks underwent minor to moderate Alpine
154 overprint with metamorphic conditions that did not exceed greenschist facies conditions
155 (Froitzheim et al., 1994; Mohn et al., 2011). To the south the Bernina - Margna - Sella -

156 Malenco nappe stack was pervasively deformed and metamorphosed reaching amphibolite
157 facies conditions during the Alpine orogeny (Figs. 2ab, 3a; see Mohn et al., 2011).

158 Previous studies (Mohn et al., 2012, 2011) recognized, from northeast to west, the
159 proximal domain, the necking zone and the distal domain of the former Adriatic margin (Figs.
160 2ab, 3) in these two distinct Alpine nappe stacks. Despite variable Alpine metamorphic
161 overprints, rift-related basement deformation has been documented in both the necking zone
162 and distal domain (Fig. 3bc) and are described below.

163 **3.1. Necking Zone: the Campo - Grosina section**

164 The former necking zone (section A-A' on Fig. 3) is composed of pre-rift upper to
165 middle crust, which is represented by the Campo and Grosina units separated by the Eita
166 Shear Zone (ESZ, Fig. 4ab; Mohn et al., 2012). The underlying Campo unit is composed of
167 amphibolite facies metasediments with a main NW-SE striking vertical foliation. These
168 metasediments are intruded by a Permian gabbroic pluton emplaced at 4-6 kbar (Sondalo
169 mafic complex, point 3; Petri et al., 2016). Importantly, the center of the Campo unit is devoid
170 of any significant post-Permian deformation (see Petri et al., 2018). The overlying Grosina
171 unit is made of amphibolite-facies orthogneiss and metasediments of unknown age showing a
172 gently NW-dipping foliation cross cut by numerous greenschist facies extensional shear zones
173 (Fig. 4cd). The ESZ represents a major shear zone that can be mapped over 20 km and is at
174 the same structural interface, i.e., between the Campo and Grosina units (Fig. 3a). Together,
175 these data suggest that the ESZ represents a horizontal mid-crustal extensional shear zone
176 with an age constrained by $^{40}\text{Ar}/^{39}\text{Ar}$ dating of porphyroclastic micas from the underlying
177 Campo unit at 205-180 Ma (Mohn et al., 2012). The rift-related P_0 -depth diagram in this
178 section is characterized by an increased pressure gradient in the Grosina unit with respect to
179 the lithostatic gradient of $0.29 \text{ kbar.km}^{-1}$.

180 The top of the Grosina unit presents a large-scale brittle detachment fault with
181 cataclasite and pseudotachylite zones corresponding to the Grosina detachment.

182 **3.2. Distal margin: Bernina – Margna – Malenco – Sella section**

183 The southern distal domain (section B-B' on Fig. 3) is composed of juxtaposed pre-rift
184 upper and lower crust as well as subcontinental mantle, represented by the Upper Margna -
185 Sella - Bernina units and the Lower Margna - Malenco units, respectively. These two distinct
186 crustal portions are separated by the Magna shear zone (Bissig and Hermann, 1999). The
187 Malenco unit is made of subcontinental mantle (section B-B', point 5), in contact with a pre-
188 rift lower crust composed of felsic granulite and sealed by the Permian Braccia gabbro (Fig.
189 4e).). The gabbro and the felsic granulite record 10-12 kbar during emplacement at 281-271
190 Ma and 8 ± 1 kbar during cooling, respectively (section B-B', points 3 and 4; Hansmann et
191 al., 2001; Müntener et al., 2000). In contrast, the pre-rift upper crust is represented by the Fora
192 gneisses (Upper Margna unit), similar to intrusive rocks from the Bernina unit that record less
193 than 3 kbar at 295-292 Ma (section B-B', point 2; Bissig and Hermann, 1999; Von Quadt et
194 al., 1994) and are covered by Permian to Triassic sediments (section B-B', point 1). Despite a
195 strong Alpine overprint, numerous localized pre-Alpine rift-related shear zones have been
196 described in the Margna unit (Müntener and Hermann, 2001). The most prominent is the
197 Margna shear zone, at the contact between the Lower Margna, including the Permian Fedoz
198 gabbro, and Upper Margna units (Fig. 4f), with a top to the E-SE sense of shear when back-
199 rotated to a pre-Alpine position (Bissig and Hermann, 1999). This structure juxtaposes pre-rift
200 rocks recording pressures of ~3 kbar against 8-12 kbar suggesting that ~25 km of continental
201 crust is lacking across this structure (Hermann and Müntener, 1996). As a result, the P_0 -depth
202 diagram of section B-B' displays a sharp gradient across the Margna shear zone highlighting
203 the absence of the middle crust and an increased gradient in the lower Margna unit.

204 In the Bernina pre-rift upper crustal unit, cataclastic structures have been recognized,
205 sometimes at the top basement and sometimes at the contact between the basement and the
206 pre-rift Triassic cover (section B-B', point 1) and are identified as the Jurassic Bernina low-
207 angle detachment fault (Mohn et al., 2011).

208 **3.3. Distal margin: Err - Platta section**

209 The northern distal margin section (section C-C' on Fig. 3) is composed of pre-rift
210 upper crust and subcontinental mantle from the Err and Platta units, respectively,
211 characterized by a set of Jurassic brittle, low-angle detachment faults referred to as the Err
212 and Jenatsch detachments (Froitzheim and Eberli, 1990; Manatschal and Nievergelt, 1997).
213 Two exhumed mantle types have been recognized in the Platta unit nowadays separated by an
214 Alpine thrust: the upper Platta, made of a sub-continental mantle (Spl-peridotite, section C-C',
215 point 4) and the lower Platta unit, made of refertilized sub-continental mantle (Spl-Pl
216 peridotite, section C-C', point 5; Müntener et al., 2010). This indicates that the two mantle
217 types followed very different thermal evolutions during rifting. The Err unit consists of
218 Permian granitoids emplaced within a polymetamorphic basement below 3 kbar at 292 ± 6
219 Ma (section C-C', point 3; Büchi, 1994; Von Quadt et al., 1994). The granitoids are covered
220 by Permian volcano-sedimentary deposits dated at 288 ± 2 Ma (section C-C', point 2; Von
221 Quadt et al., 1994). In contrast to the Bernina - Margna - Malenco - Sella nappe stack, no
222 evidence for pre-rift lower crust has been recognized in this section. The top of the Err unit is
223 generally capped by a low-angle Jurassic detachment fault locally following the base of
224 Permian basins filled by volcanoclastic deposits (Fig. 4gh; Epin et al., 2017; Masini et al.,
225 2011). The contact between Lower Err and Upper Platta is interpreted as an Alpine thrust,
226 potentially reactivating a former Jurassic rift related structure (Epin et al., 2017). In a P_0 -depth
227 diagram, the transition between points 3 and 4 involves a possible sharp gradient resulting
228 from the absence of middle and lower continental crust.

229 4. THE SOUTHERN ALPS CASE STUDY

230 The Southern Alps are delimited by the Tertiary Insubric Line to the northwest and by
231 the Pô plain to the south (Figs. 2ac, 5, 6). They are composed at their western end by two
232 major units: the pre-rift middle to lower crustal Ivrea-Verbano Zone (IVZ), recording the
233 emplacement of a Permian mafic complex within a polymetamorphic basement, and the pre-
234 rift upper crustal Serie Dei Laghi (SDL), capped to the southeast by Permian to Mesozoic
235 sediments of the Lombardian basin. Whereas the IVZ is exhumed and tilted to $\sim 90^\circ$ by the
236 time of Jurassic rifting and the Alpine compression (Siegesmund et al., 2008), the SDL and its
237 associated sedimentary cover show only minor Alpine deformation and metamorphic
238 overprint (i.e. lower greenschist facies condition).

239 The Southern Alps record evidence for long-lasting extension that started in the Late
240 Triassic and shifted progressively westward during the Middle Jurassic (Bertotti et al., 1993).
241 To the east, fault-bounded rift basins such as the Lombardian basin are filled by shallow-
242 water Triassic to Jurassic deposits representing the Adriatic proximal margin (Fig. 5b; Bertotti
243 et al., 1993). The SDL – IVZ are interpreted as the Adriatic necking zone recording major
244 thinning during Jurassic rifting (Decarlis et al., 2017). The distal domain is preserved in the
245 Canavese zone with evidence for subcontinental mantle exhumation at the seafloor (Beltrando
246 et al., 2015a; Ferrando et al., 2004).

247 Several deep-crustal extensional structures have been documented in the SDL and the
248 IVZ. The oldest, the Cossato-Mergozzo-Brissago line (CMB) was active during the Permian
249 without evidence for subsequent reactivation and delimits, in places, the SDL from the IVZ
250 (Mulch et al., 2002b). Conversely, two sets of structures interpreted as related to Mesozoic
251 rifting have been documented in the IVZ: (1) deep, high-temperature shear zones such as the
252 Anzola-Rosarolo Shear Zone (ARSZ; e.g. Langone et al., 2018) and (2) the shallower Pogallo
253 Line (PL), marking in places also the contact between the SDL and the IVZ. These structures

254 are described below using three sections that illustrate the partitioning of rift-related
255 deformation in the pre-rift lower crust (Fig. 5bc). The IVZ being presently tilted to $\sim 90^\circ$, the
256 P_0 -depth diagrams can be approximated by P_0 versus the distance to the Tertiary Insubric line
257 (i.e. moving towards this structure, rocks were deeper in pre-rift crustal section).

258 **4.1. Val Sesia section**

259 The Val Sesia and Val Sessera sections (D-D' on Fig. 5) are composed of Permian
260 gabbros and diorites of the Ivrea Mafic Complex with metasedimentary and peridotite lenses
261 capped by upper amphibolite-facies metasediments (Quick et al., 2003). A dense dataset of
262 Permian P - T estimates derived from both igneous and metamorphic rocks define a P_0 -distance
263 gradient of $0.36 \text{ kbar.km}^{-1}$ (Demarchi et al., 1998). Igneous and metamorphic textures are
264 usually preserved whereas only rare and minor shear zones, potentially related to Jurassic
265 rifting, have been described in this section (Altenberger, 1997).

266 **4.2. Val Strona section**

267 The Val Strona section (E-E' on Fig. 5) is composed of gabbroic dykes and
268 amphibolite to granulite facies metasedimentary rocks. This section preserved pre-Triassic
269 structures, crosscut by several shear zones at distinct crustal levels that are rarely dated. The
270 closest to the Insubric line (i.e., the deepest in a reconstructed section), the meters-thick
271 ARSZ (Fig. 6ab) presents syn-deformational amphibolite to granulite facies conditions (> 650
272 $^\circ\text{C}$) and is dated at 210-200 Ma (Beltrando et al., 2015b; Brodie et al., 1989). Up-section,
273 above the Permian CMB, the PL is the second major rift-related structure outcropping in the
274 Val Strona section (Fig. 6c). It appears as a tilted ductile shear zone dated at $182 \pm 2 \text{ Ma}$
275 (Mulch et al., 2002a) with greenschist facies deformation (Handy, 1987). As a result Permian
276 P - T conditions overprinted by these successive rift-related deformations define a P_0 -depth
277 gradient of $0.42 \text{ kbar.km}^{-1}$ (Henk et al., 1997).

278 **4.3. Valle Cannobina section**

279 In the Valle Cannobina (F-F' on Fig. 5), two major high grade deformation zones
280 (Finero Shear Zones; FSZ) separate the Upper amphibolite-facies metasediments (i.e. the
281 Kinzigite formation), the so-called external gabbro from the “layered internal zone” and
282 associated mantle peridotite (Kenkmann and Dresen, 2002) leaving the contact between the
283 “layered internal zone” and the mantle peridotites (i.e., the petrological Moho) undeformed.
284 The shear zones were active at high temperature (>650 °C), record a normal sense of shear
285 and are dated at 235-200 Ma (Langone et al., 2017, 2018). Further away from the Insubric
286 line, the PL presents amphibolite-facies deformations (Handy, 1987). Altogether, the shear
287 zones juxtapose mantle peridotites, upper and lower crustal rocks on a few kilometers
288 distance, resulting in an extremely high P_0 -depth gradient of 1.8 kbar.km⁻¹ (Handy et al.,
289 1999). This indicates that major crustal thinning occurred at 235-200 Ma along this transect
290 (Handy et al., 1999; Langone et al., 2018) whereas no deformation was documented in the
291 upper-crustal SDL.

292 **5. NUMERICAL MODELING**

293 **5.1. Modeling approach**

294 In order to unravel the impact of mechanical heterogeneities on the structuring and
295 architecture of rifted margins, we have designed a set of thermo-mechanical numerical
296 models. The two-dimensional models were carried out at the scale of the continental
297 lithosphere and incorporated discrete km-scale elliptical bodies of differing rheologies that
298 represent inherited lithological variations. The modeling approach is based on a finite
299 difference/marker-in-cell discretization of the momentum and heat transfer equations (Gerya
300 and Yuen, 2003). The numerical algorithm has the ability to simulate the evolution of a true
301 free surface (Duretz et al., 2016a) and combines, in a consistent manner, a variety of

302 rheological behaviors (elasticity, viscosity, plasticity) and creep mechanisms (Popov and
303 Sobolev, 2008; Schmalholz and Duretz, 2017). See Text S3 for details.

304 **5.2. Model configuration**

305 The initial model domain is 300 km wide and 120 km high (Fig. 7a). Extension is
306 applied by prescribing horizontal velocities at the lateral model boundaries (left, right,
307 bottom), satisfying a constant bulk extension rate of 10^{-15} s^{-1} . The models were run with a
308 numerical resolution of 150 x 75 m (2000 x 1600 cells) and a Courant number of 0.5 for the
309 adaptive time step (i.e. the maximum displacement per time step is half a grid space). The top
310 of the model is a free surface on which the action of surface processes is not taken into
311 account. The initial thermal field is that of an equilibrium field that includes radiogenic heat
312 production in the continental crust and exhibits 500-550 °C at the Moho. Zero heat flow
313 boundary conditions are prescribed at the lateral sides of the model; the top and bottom
314 boundaries are characterized by a constant temperature (0 and 1330 °C, respectively). The
315 continental crust is initially 30 km thick and is modelled with a visco-plastic layer of
316 moderate strength (anorthite flow law; Rybacki and Dresen, 2004) and includes embedded
317 elliptical bodies of relatively weaker (4 x 67 km ellipses; wet quartzite; Kirby, 1983) and
318 stronger rheologies (4-7 x 42-77 km ellipses; Maryland diabase; Mackwell et al., 1998)
319 representing laterally discontinuous strength variations mimicking structural or lithological
320 heterogeneities. Weak ellipses mimic rheological weak lithologies such as phyllosilicate-rich
321 metasedimentary units in upper and mid-crustal position (e.g. Grosina and the Serie dei Laghi
322 units), whereas strong ellipses stand for rheological strong lithologies such as mid-crustal
323 (Sondalo mafic complex) and lower crustal mafic intrusions (Braccia and Ivrea mafic
324 complexes). The upper subcontinental mantle is initially 40 km thick and is modelled using a
325 visco-plastic layer dominated by dry olivine (Carter and Tsenn, 1987) and incorporates
326 weaker lens-shaped bodies dominated by wet olivine (3 x 61 km ellipses; Carter and Tsenn,

327 1987) to model heterogeneities in the mantle (e.g. pre-existing petro-fabric, modal variations,
328 crystallized melt pockets). The lower subcontinental mantle is modelled using a purely
329 viscous layer dominated by a wet olivine rheology. No prescribed strain-softening
330 parameterization is applied in the models, the numerical models are hence less prone to mesh-
331 dependence and exhibit a good convergence upon mesh refinement (see Figure S5). The
332 models are also performed using different initial lithospheric structures (see Text S3, Table S4
333 and Figure S6).

334 **5.1. Modeling results: reference model**

335 The geometrical and rheological evolution of the reference model is depicted in Figs. 7
336 and 8 (see also Movies S8-S10). Within the first 10% of extension, the deformation of the
337 continental crust is distributed and mainly in the frictional field. The main localizing feature is
338 the weak inclusion originally positioned at about 20 km depth that acts as a *décollement* level
339 in the ductile field (Fig. 8a). The deformation of the upper subcontinental mantle gives rise to
340 an overall necking pattern (Fig. 7b). Some localized deformation occurs close to the Moho
341 where the stronger mantle reaches conditions of frictional deformation and undergoes necking
342 in the regions where heterogeneities induce a local stratification (Fig. 8a). After about 15% of
343 extension, the upper subcontinental mantle is almost totally necked and devoid of any
344 frictional deformation (Fig. 7c, 8b). The activation of numerous frictional shear bands in the
345 crust leads to the formation of a pattern of tilted blocks (Fig. 7c). The stronger heterogeneities
346 present in the crust are still mostly undeformed compared to surrounding material. After 25%
347 of extension, the upper subcontinental mantle is fully necked although the crust in the center
348 of the rift is still about 15 km thick (Fig. 7d). As the initially deep mantle is in direct contact
349 with the crust, the Moho temperature rises to about 600 °C. Frictional deformation is only
350 activated in the crust and occurs on a few shear bands only (Fig. 8c). One frictional structure
351 propagates across the strong central heterogeneity and shears it apart, forming an apparent

352 large scale pinch and swell structure (Fig. 7d and 8c). The conditions of extreme crustal
353 thinning and final crustal breakup occur after 30% of extension (Fig. 7e). The final necking
354 migrates basinwards (towards the center of the model) due to the presence of the strong
355 central crustal heterogeneity. As the mantle flows closer to the surface, it cools down below
356 600 °C and reaches the conditions of frictional deformation. As most of the deformation
357 occurs now in the upper subcontinental mantle, the two continental margins do not undergo
358 any further prominent strain (Fig. 8d) while deformation is only accommodated by creep of
359 the lower subcontinental mantle.

360 **5.2. Modeling results: impact of rheological contrasts**

361 The impact of tectonic inheritance is a direct consequence of the strength contrasts
362 between different lithologies. For example, the extension of a small scale multilayer material
363 with negligible strength contrasts may likely not undergo any localized necking (see
364 Schmalholz and Mancktelow, 2016). In order to investigate the impact of strength variations,
365 we systematically increased and decreased the strength contrasts between the crust, mantle
366 and their heterogeneities. To do so, we artificially varied ductile flow strength of the
367 heterogeneities (Fig. 9). Increasing the effective viscosity of weak heterogeneities and
368 reducing the viscosity of strong heterogeneities by a factor of 10 simulated small strength
369 contrasts (Fig. 9a). Conversely, decreasing the viscosity of weak heterogeneities and
370 increasing the viscosity of strong heterogeneities by a factor of 10 simulated large strength
371 contrasts (Fig. 9c). These models were compared to the reference model (Fig. 9b) for similar
372 amounts of extension (40%). The model with low strength contrast clearly differs from the
373 reference model (Fig. 9ab). It is dominated by a distributed thinning of the lithosphere
374 ultimately leading to a single lithosphere-scale necking (Chenin et al., 2018; Fletcher and
375 Hallett, 1983). The model with large strength contrast resembles the reference model but

376 exhibits much more localized features (Fig. 9bc). The tilted-block pattern in the upper crust is
377 amplified and the overall rift asymmetry is more pronounced.

378 **6. DISCUSSION**

379 The comparison of both field observations from the remnants of the Alpine Tethys and
380 numerical models led to characterize the different structures accommodating the thinning of
381 the continental lithosphere in relation with initial heterogeneities. The detailed comparison
382 between the Alpine Tethys rifted margin architecture based on field observations, the
383 numerical modelling results and related P_0 -depth diagrams are provided in Figure S7.

384 **6.1. Distribution of deformation across the rifted margin**

385 *6.1.1. The proximal domain*

386 From the proximal to the distal domains, the style of extensional structures
387 significantly changes. In the proximal domain, most of the extension is accommodated by
388 high-angle normal faults essentially developed during the early rifting stage (Fig. 8ab). These
389 faults are generally able to cut across the brittle upper crust before soling into *décollement*
390 levels. Such *décollement* levels may be localized either at the brittle-ductile transition at mid-
391 crustal depth or in weak lithologies (e.g., phyllosilicate-rich layers). In contrast, the
392 deformation of the deepest part of the crust appears to be accommodated by diffuse ductile
393 deformation. At that stage, P_0 -depth diagrams are weakly modified ($0.32 \text{ kbar.km}^{-1}$) with
394 respect to a normal lithostatic gradient (max. $0.29 \text{ kbar.km}^{-1}$; Fig. 10fg) emphasizing the weak
395 crustal thinning recorded in this domain. This is in agreement with the low accommodation
396 space deduced from the syn- to post-rift sedimentary record (e.g. Eberli, 1988).

397 **6.1.2. The necking zone**

398 The deformation style evolves across the necking zone in association with an increase
399 of crustal thinning. Most of the normal faults affecting the upper crust are progressively
400 rooting on a major *décollement* that can be followed until the development of the proximal
401 domain. At depth, small-scale necking of individual strong layers allows *décollement* levels to
402 connect different crustal levels. Strong layers remain almost undeformed while most of the
403 deformation localizes in surrounding, weak lithologies, conditioning the system for lateral
404 extraction (see section 6.3). In particular the ESZ may represent an example of a *décollement*,
405 delimiting the essentially undeformed Campo unit hosting pre-rift Permian gabbroic
406 intrusions from the overlying, deformed Grosina unit (A-A'). This is similar to lateral
407 variations in lower crustal strain documented in the Southern Alps (Fig. 5). The pre-rift mafic
408 intrusion of the lower crustal IVZ, recorded weak to no rift-related deformation while P_0 -
409 depth gradient is almost unmodified with respect to the lithostatic gradient. However,
410 deformation increases in the surrounding metasediments where several rift-related shear zones
411 have been recognized (Figs. 5, 6). The presence of these shear zones is associated with
412 modifications in P_0 -depth gradients from $0.42 \text{ kbar.km}^{-1}$ close to the main mafic complex in
413 Val Strona (E-E') up to 1.8 kbar.km^{-1} in Val Cannobina (F-F', Fig. 5d). This strain
414 partitioning, both vertically and laterally, is well illustrated in the synthetic P_0 -depth diagrams
415 across the necking zone (Fig. 10de) where both the crust and the mantle are characterized by
416 various P_0 -depth gradients resulting from the incipient lateral extraction of distinct portions of
417 the continental basement (see section 6.3). As an example, the lower crust in the necking zone
418 may either be weakly deformed, surrounded by high-strain zones with high local P_0 -depth
419 gradients ($0.43 \text{ kbar.km}^{-1}$ to $2.87 \text{ kbar.km}^{-1}$, Fig. 10e) or pervasively deformed with high P_0 -
420 depth gradients ($1.18 \text{ kbar.km}^{-1}$, Fig. 10d). With more extension, deformation at the surface

421 starts to be localized along few major detachment faults that remain restricted to the crust
422 whereas the deformation stops in this domain at around 25% (Fig. 8cd).

423 **6.1.3. The distal domain**

424 In the distal domain, highly extended continental crust passes laterally to
425 subcontinental mantle exhumed at the seafloor. Normal faults cutting across the entire
426 residual crust sole into a *décollement* now coinciding with the Moho (Fig. 8ab). Such a
427 configuration has been described in the present-day Iberia margin and identified as the S-
428 reflector (Reston et al., 1996). Deep deformation in this domain is extremely localized: high-
429 strain zones are distributed in initially weak lithologies while strong lithologies remain almost
430 undeformed. Such strain partitioning is explained by the lateral extraction (see section 6.3) of
431 strong layers from the future distal domain during the early extensional stages (Fig. 7). This
432 lateral extraction appears as an efficient process able to thin the continental crust over few
433 kilometers. As this process occurs during extension, local thickening caused by extraction of
434 lateral levels is inhibited. Similar to the continental crust, the mantle is rapidly necked by the
435 interaction of large offset normal faults and *décollement* levels. The direct implication of fully
436 achieved lateral extraction for the associated P_0 -depth diagram is the presence of sharp
437 gradients of P_0 with depth surrounding preserved domains ($0.42 \text{ kbar.km}^{-1}$, Fig. 10c). This is
438 also reported for the two distal margin examples in the Eastern Alps (Fig. 3). In the southern
439 distal margin (C-C'), the pre-rift upper and lower crusts are juxtaposed via the Margna shear
440 zone (Figs. 3, 4ef). In this context, the Margna shear zone represents an extraction fault that
441 remains after the extraction of mid-crustal units. Eventually, deformation localizes along main
442 detachment faults with increasing strain amount to finally exhume at the seafloor deep levels
443 such as the mantle (Figs. 7, 8).

444 **6.2. The role of heterogeneities**

445 Our observations and numerical models indicate that initial mechanical heterogeneities
446 have a first-order control on the mechanisms of thinning and eventually on the evolution and
447 architecture of rifted margins. Among others, the relative strength contrasts between the
448 heterogeneities and their initial position in the continental lithosphere are key parameters.

449 For small rheological contrasts (effective viscosity contrast decreased by a factor of
450 10; see Table S4 for reference rheological parameters), deformation is highly distributed over
451 the entire section (Fig. 9) and the necking of both the mantle and the crust are symmetrical.
452 This setting leads to the formation of a wide zone of lithospheric thinning, delaying or even
453 inhibiting mantle exhumation. In contrast, moderate and large strength contrasts (reference
454 model or effective viscosity contrast increased by a factor of 10) rapidly partition the
455 deformation in weak lithologies: decoupling levels may be active over large distances across
456 the margin and their lifetime may also be protracted. Strain partitioning triggers the lateral
457 extraction of the strong parts of the crust or mantle that remains weakly deformed to
458 undeformed. The removal of the strong layers permits the connection of weak layers by
459 extensional structures leading to the mechanical coupling of the crust and the mantle and
460 permits exhumation of the latter to the seafloor. Our model does not integrate decompression
461 melting which, if arriving early enough with respect to crustal thinning, may abort mantle
462 exhumation at the seafloor (Davis and Lavier, 2017; Larsen et al., 2018; Ros et al., 2017;
463 Tugend et al., 2018). In general, significant rheological contrasts favour mantle exhumation
464 and less total strain is requested (Fig. 9). Finally, the detachment fault responsible for
465 exhumation generates a margin asymmetry.

466 The initial vertical and horizontal position of heterogeneities also has implications for
467 the distribution of the extensional deformation (see also Figure S6). At the lithospheric scale,
468 the role of heterogeneities seems to be negligible at the shallowest levels; high-angle brittle

469 structures are generated independent of the position of heterogeneities but may still be locally
470 controlled by inherited structures. Upper crustal heterogeneities are therefore behaving as
471 passive markers of the deformation. In contrast, the development of deep deformation bands
472 in the ductile regime is strongly controlled (in case of sufficient strength contrast) by the
473 presence of weak lithologies localizing the deformation or strong lithologies forcing
474 deformation either to shallower or deeper levels. This is notably the case for *décollement*
475 levels onto which normal faults sole.

476 From both field observations and numerical models, we show that at the scale of the
477 lithosphere, deformation is preferentially localized in initially weak lithologies, affecting to a
478 lesser extent initially strong lithologies (see Figure S7). The most important parameter is the
479 rheological contrast between two lithologies and not their absolute rheological parameters
480 (e.g. Handy, 1994). Examples for weak lithologies could be phyllosilicate-rich (meta-)
481 sediments with a pre-rift foliation (Shea and Kronenberg, 1993) or granitoids while strong
482 lithologies could be mafic intrusions. The necking zone of the Eastern Alps best exemplifies
483 this relation: the Grosina unit, which is made of metasediment and orthogneiss derived from
484 granitoid, localizes several rift-related structures, whereas the underlying Sondalo gabbroic
485 complex and surrounding Campo unit escaped rift-related deformation. Granitoids may even
486 be the weakest lithologies in case of a more mafic continental crust. Once rifting is initiated,
487 several mechanisms may further enhance weakening of the deforming zone by grain size
488 reduction (Fitz Gerald and Stünitz, 1993; Handy, 1990), metamorphic retrogression (Wintsch
489 et al., 1995), shear heating (Brun and Cobbold, 1980) or formation of petrofabric (Holyoke
490 and Tullis, 2006).

491 **6.3. The importance of heterogeneity-enhanced extraction tectonics**

492 The incorporation of heterogeneities highlights that extraction tectonics represent an
493 efficient manner to accommodate lithospheric thinning. As exemplified by Froitzheim et al.

494 (2006), it requires to localize the deformation in conjugate shear zones surrounding an
495 undeformed to weakly deformed volume. Shear zones have opposite sense of displacement
496 and are connected at the tip of the volume, leaving an extraction fault or shear zone behind
497 (see Fig. 1 of Froitzheim et al., 2006). In extensional tectonic systems, this extraction fault
498 may record a complex sense of motion and amount of strain (Froitzheim et al., 2006). Such
499 mechanisms have been proposed to exist in the extending continental lithosphere, either in
500 late- to post-orogenic systems (Fossen et al., 2014) or during the formation of extremely
501 extended margins (Clerc and Lagabrielle, 2014; Froitzheim et al., 2006; Mohn et al., 2012).

502 Lateral extraction is thus a viable mechanism only in case of depth-dependent
503 thinning, likely activated if kilometre-scale, laterally discontinuous heterogeneities are
504 present. In the models (Figs. 7-10), the heterogeneities pre-set the system to enhance
505 extraction. However, lateral discontinuity can also be generated during extension. As shown
506 by Brun and Beslier (1996) and Duretz et al. (2016b), initially strong and continuous layers
507 may be necked to form individual large-scale boudins that are conducive to extraction by
508 continuous extension.

509 Field examples of this necking-related mechanism are well documented in the Eastern
510 Alps. Whereas distal-most domains are showing examples in which extraction has been
511 completed, aborted extraction can be seen in the necking zone (Figs. 3, 5). Indeed, the ESZ
512 affects the orthogneissic Grosina unit, leaving undeformed the underlying Campo unit, which
513 hosts a Permian gabbro inhibiting deformation in the latter unit. Such observations show the
514 control of pre-existing lithologies on the partitioning of deformation and led to the selection
515 of different extraction levels during rifting. Hence, the finite result of extreme lithospheric
516 thinning is the juxtaposition of internally weakly to undeformed sections of the continental
517 lithosphere. These sections are juxtaposed across complex extensional high-strain zones that
518 act either as decoupling horizons with relatively horizontal geometries or variably inclined

519 structures. Such processes explain the preservation of pre-rift fabric and lithology in
520 extremely thinned continental crust.

521 **6.4 Implications for present-day rifted margins**

522 This study suggests that, at least locally, the discrepancy between recognized faulting
523 and observed total crustal thinning is the result of a complex interplay between intra-basement
524 deformation zones. Several contributions have already emphasized the role of boudinage in
525 present-day margins as for instance documented offshore Britain (Reston, 1988). Our results
526 further explain the composition of extremely thinned distal domains; depending on the initial
527 architecture of continental lithosphere, various crustal levels can be extracted from the future
528 distal domain. This domain may therefore be composed of a juxtaposition of different crustal
529 levels with different pre-rift and syn-rift *P-T* histories. As consequence even in the most distal
530 margins, undeformed pre-rift crustal levels can therefore be preserved, surrounded by rift-
531 related extensional structures. In the Iberia-Newfoundland rifted margin, the distal domain
532 was interpreted to be the result of the juxtaposition of both upper and lower crust inferred
533 from both drilling results and seismic surveys (e.g. Péron-Pinvidic and Manatschal, 2009). In
534 contrast, the exhumation of the lower crust was proposed in parts of the SW Barents sea
535 (Gernigon et al., 2014), the Gulf of Lion (Jolivet et al., 2015) or offshore Gabon (Clerc et al.,
536 2018).

537 **7. CONCLUSION**

538 We investigated the control of initial mechanical heterogeneities such as changing
539 lithologies, inherited mechanical anisotropies (e.g., rock fabrics) or pre-rift structures on the
540 rifting kinematics and dynamics.

541 The pre-rift architecture of the continental lithosphere was reconstructed from field
542 observations in the remnants of the Alpine Tethys. The evolution of the different portions of

543 the continental lithosphere was tracked during the rifting by studying initial pressure (P_0) –
544 depth diagrams highlighting the homogenous thinning or missing distinct pre-rift levels of the
545 lithosphere.

546 We compared these observations to two-dimensional thermo-mechanical numerical
547 models investigating the role of initial lithospheric heterogeneities for the architecture and
548 evolution of rifted margins. The style of lithospheric extension is strongly influenced by the
549 rheological contrasts between the embedded heterogeneities within the continental crust /
550 lithosphere.

551 These multidisciplinary approaches emphasized the critical role of extraction tectonics
552 that appears as an efficient mechanism to thin the continental lithosphere. Such mechanism
553 initiates in the necking zone, recording strong variations in strain distribution, both vertically
554 and horizontally. As a consequence, the deep deformation in the distal domain is localized
555 along high-strain zones left behind after extraction of various strong levels. Depending on the
556 initial position of the heterogeneities, different levels may be selected for lateral extraction
557 during rifting, explaining the variable composition of distal margin basement.

558 **ACKNOWLEDGMENT**

559 The authors thank Antonio Langone, Gianreto Manatschal, Patricio Figueredo and
560 Christopher Johnson for discussions as well as Lin Chen and an anonymous referee for their
561 reviews. This work is dedicated to Marco Beltrando.

562 **FUNDING**

563 This work was supported by the University of Lausanne and an ExxonMobil research
564 grant to BP and OM.

565 **SUPPORTING INFORMATION**

566 **Supplementary material 1**

567 **Table S1.** Compilation of published P - T - t estimates from the Eastern Alps

568 **Table S2.** Compilation of published P - T - t estimates from the Southern Alps and associated
569 statistics

570 **Text S3.** Modelling methodology and parameters

571 **Table S4.** Summary of thermal and rheological parameters used in the numerical experiments

572 **Figure S5.** Model resolution tests

573 **Figure S6.** Additional numerical models

574 **Figure S7.** P ₀-depth summary figure

575 **Supplementary material 2**

576 **Movie S8.** Reference model with phase coloring

577 **Supplementary material 3**

578 **Movie S9.** Accumulated strain of the reference model

579 **Supplementary material 4**

580 **Movie S10.** Frictional and ductile strain rate of the reference model

581 **REFERENCES**

- 582 Altenberger, U., 1997. Strain localization mechanisms in deep-seated layered rocks. *Geol.*
583 *Rundschau* 86, 56–68. doi:10.1007/s005310050121
- 584 Beltrando, M., Compagnoni, R., Ferrando, S., Mohn, G., Frasca, G., Odasso, N.,
585 Vokmanović, Z., Masini, E., 2015a. Crustal thinning and mantle exhumation in the
586 Levone area (Southern Canavese Zone, Western Alps), in: *A Field Guide Across the*
587 *Margins of Alpine Tethys*, J. Virtual Explor., Vol. 48, Edited by G. Manatschal et Al.
588 doi:10.3809/jvirtex.2013.00326.
- 589 Beltrando, M., Manatschal, G., Mohn, G., Dal Piaz, G. V, Vitale Brovarone, A., Masini, E.,
590 2014. Recognizing remnants of magma-poor rifted margins in high-pressure orogenic
591 belts: The Alpine case study. *Earth-Science Rev.* 131, 88–115.
592 doi:10.1016/J.EARSCIREV.2014.01.001
- 593 Beltrando, M., Stockli, D.F., Decarlis, A., Manatschal, G., 2015b. A crustal-scale view at rift
594 localization along the fossil Adriatic margin of the Alpine Tethys preserved in NW Italy.
595 *Tectonics* 34, 1927–1951. doi:10.1002/2015TC003973
- 596 Beltrando, M., Zibra, I., Montanini, A., Tribuzio, R., 2013. Crustal thinning and exhumation
597 along a fossil magma-poor distal margin preserved in Corsica: A hot rift to drift
598 transition? *Lithos* 168–169, 99–112. doi:http://dx.doi.org/10.1016/j.lithos.2013.01.017
- 599 Bertotti, G., Picotti, V., Bernoulli, D., Castellarin, A., 1993. From rifting to drifting: tectonic
600 evolution of the South-Alpine upper crust from the Triassic to the Early Cretaceous.
601 *Sediment. Geol.* 86, 53–76. doi:http://dx.doi.org/10.1016/0037-0738(93)90133-P
- 602 Bissig, T., Hermann, J., 1999. From pre-Alpine extension to Alpine convergence: the example
603 of the southwestern margin of the Margna nappe (Val Malenco, N-Italy). *Schweizerische*
604 *Mineral. und Petrogr. Mitteilungen* 79, 363–380.
- 605 Brodie, K.H., Rex, D., Rutter, E.H., 1989. On the age of deep crustal extensional faulting in
606 the Ivrea zone, northern Italy. *Geol. Soc. London, Spec. Publ.* 45, 203–210.
- 607 Brun, J.P., Beslier, M.O., 1996. Mantle exhumation at passive margins. *Earth Planet. Sci.*
608 *Lett.* 142, 161–173. doi:http://dx.doi.org/10.1016/0012-821X(96)00080-5
- 609 Brun, J.P., Cobbold, P.R., 1980. Strain heating and thermal softening in continental shear
610 zones: a review. *J. Struct. Geol.* 2, 149–158. doi:10.1016/0191-8141(80)90045-0
- 611 Büchi, H., 1994. Der variskische Magmatismus in der östlichen Bernina. *Schweizerische*
612 *Mineral. und Petrogr. Mitteilungen* 74, 359–371.
- 613 Carter, N.L., Tsenn, M.C., 1987. Flow properties of continental lithosphere. *Tectonophysics*
614 136, 27–63. doi:https://doi.org/10.1016/0040-1951(87)90333-7
- 615 Clerc, C., Jolivet, L., Ringenbach, J.-C., 2015. Ductile extensional shear zones in the lower
616 crust of a passive margin. *Earth Planet. Sci. Lett.* 431, 1–7.
617 doi:http://dx.doi.org/10.1016/j.epsl.2015.08.038
- 618 Clerc, C., Lagabrielle, Y., 2014. Thermal control on the modes of crustal thinning leading to
619 mantle exhumation: Insights from the Cretaceous Pyrenean hot paleomargins. *Tectonics*
620 33, 1340–1359.
- 621 Clerc, C., Ringenbach, J.-C., Jolivet, L., Ballard, J.-F., 2018. Rifted margins: Ductile
622 deformation, boudinage, continentward-dipping normal faults and the role of the weak
623 lower crust. *Gondwana Res.* 53, 20–40. doi:https://doi.org/10.1016/j.gr.2017.04.030
- 624 Chenin, P., Schmalholz, S.M., Manatschal, G., Karner, G.D., 2018. Necking of the
625 Lithosphere: A Reappraisal of Basic Concepts With Thermo-Mechanical Numerical
626 Modeling. *J. Geophys. Res. Solid Earth* 123, 5279–5299. doi:10.1029/2017JB014155
- 627 Davis, J.K., Lavier, L.L., 2017. Influences on the development of volcanic and magma-poor
628 morphologies during passive continental rifting. *Geosphere* 13, 1524–1540.
629 doi:10.1130/GES01538.1

630 Decarlis, A., Beltrando, M., Manatschal, G., Ferrando, S., Carosi, R., 2017. Architecture of
631 the Distal Piedmont-Ligurian Rifted Margin in NW Italy: Hints for a Flip of the Rift
632 System Polarity. *Tectonics* 36, 2388–2406. doi:10.1002/2017TC004561

633 Demarchi, G., Quick, J.E., Sinigoi, S., Mayer, A., 1998. Pressure gradient and original
634 orientation of a lower-crustal intrusion in the Ivrea-Verbano zone, Northern Italy. *J.*
635 *Geol.* 106, 609–622.

636 Dewey, J.F., Bird, J.M., 1970. Mountain belts and the new global tectonics. *J. Geophys. Res.*
637 75, 2625–2647. doi:10.1029/JB075i014p02625

638 Duretz, T., May, D.A., Yamato, P., 2016a. A free surface capturing discretization for the
639 staggered grid finite difference scheme. *Geophys. J. Int.* 204, 1518–1530.

640 Duretz, T., Petri, B., Mohn, G., Schmalholz, S.M., Schenker, F.L., Müntener, O., 2016b. The
641 importance of structural softening for the evolution and architecture of passive margins.
642 *Sci. Rep.* 6, 38704. doi:10.1038/srep38704

643 Eberli, G.P., 1988. The evolution of the southern continental margin of the Jurassic Tethys
644 Ocean as recorded in the Allgäu Formation of the Austroalpine Nappes of Graubünden
645 (Switzerland). *Eclogae Geol. Helv.* 81, 175–214.

646 Epin, M.-E., Manatschal, G., Amann, M., 2017. Defining diagnostic criteria to describe the
647 role of rift inheritance in collisional orogens: the case of the Err-Platta nappes
648 (Switzerland). *Swiss J. Geosci.* 110, 419–438. doi:10.1007/s00015-017-0271-6

649 Ferrando, S., Bernoulli, D., Compagnoni, R., 2004. The Canavese zone (internal Western
650 Alps): a distal margin of Adria. *Schweizerische Mineral. und Petrogr. Mitteilungen* 84,
651 237–256.

652 Fitz Gerald, J.D., Stünitz, H., 1993. Deformation of granitoids at low metamorphic grade. I:
653 Reactions and grain size reduction. *Tectonophysics* 221, 269–297. doi:10.1016/0040-
654 1951(93)90163-E

655 Fletcher, R.C., Hallet, B., 1983. Unstable extension of the lithosphere: A mechanical model
656 for basin-and-range structure. *J. Geophys. Res. Solid Earth* 88, 7457–7466.
657 doi:10.1029/JB088iB09p07457

658 Fossen, H., Gabrielsen, R.H., Faleide, J.I., Hurich, C.A., 2014. Crustal stretching in the
659 Scandinavian Caledonides as revealed by deep seismic data. *Geol.* .

660 Fountain, D.M., Salisbury, M.H., 1981. Exposed cross-sections through the continental crust:
661 implications for crustal structure, petrology, and evolution. *Earth Planet. Sci. Lett.* 56,
662 263–277. doi:http://dx.doi.org/10.1016/0012-821X(81)90133-3

663 Frasca, G., Gueydan, F., Brun, J.-P., Monié, P., 2016. Deformation mechanisms in a
664 continental rift up to mantle exhumation. Field evidence from the western Betics, Spain.
665 *Mar. Pet. Geol.* 76, 310–328. doi:http://dx.doi.org/10.1016/j.marpetgeo.2016.04.020

666 Froitzheim, N., Eberli, G.P., 1990. Extensional detachment faulting in the evolution of a
667 Tethys passive continental margin, Eastern Alps, Switzerland. *Geol. Soc. Am. Bull.* 102,
668 1297–1308. doi:10.1130/0016-7606(1990)102<1297:edfite>2.3.co;2

669 Froitzheim, N., Pleuger, J., Nagel, T.J., 2006. Extraction faults. *J. Struct. Geol.* 28, 1388–
670 1395. doi:https://doi.org/10.1016/j.jsg.2006.05.002

671 Froitzheim, N., Schmid, S.M., Conti, P., 1994. Repeated change from crustal shortening to
672 orogen-parallel extension in the Austroalpine units of Graubünden. *Eclogae Geol. Helv.*
673 87, 559–612.

674 Gernigon, L., Brönnner, M., Roberts, D., Olesen, O., Nasuti, A., Yamasaki, T., 2014. Crustal
675 and basin evolution of the southwestern Barents Sea: From Caledonian orogeny to
676 continental breakup. *Tectonics* 33, 347–373. doi:10.1002/2013TC003439

677 Gerya, T. V., Yuen, D.A., 2003. Characteristics-based marker-in-cell method with
678 conservative finite-differences schemes for modeling geological flows with strongly
679 variable transport properties. *Phys. Earth Planet. Inter.* 140, 293–318.

680 doi:<https://doi.org/10.1016/j.pepi.2003.09.006>

681 Handy, M.R., 1987. The structure, age and kinematics of the Pogallo Fault Zone; Southern
682 Alps, northwestern Italy. *Eclogae Geol. Helv.* 80, 595–632.

683 Handy, M.R., 1990. The solid-state flow of polymineralic rocks. *J. Geophys. Res.* 95, 8647.
684 doi:[10.1029/JB095iB06p08647](https://doi.org/10.1029/JB095iB06p08647)

685 Handy, M.R., 1994. Flow laws for rocks containing two non-linear viscous phases: A
686 phenomenological approach. *J. Struct. Geol.* 16, 287–301. doi:[10.1016/0191-
687 8141\(94\)90035-3](https://doi.org/10.1016/0191-8141(94)90035-3)

688 Handy, M.R., Franz, L., Heller, F., Janott, B., Zurbriggen, R., 1999. Multistage accretion and
689 exhumation of the continental crust (Ivrea crustal section, Italy and Switzerland).
690 *Tectonics* 18, 1154–1177. doi:[10.1029/1999tc900034](https://doi.org/10.1029/1999tc900034)

691 Hansmann, W., Müntener, O., Hermann, J., 2001. U-Pb zircon geochronology of a tholeiitic
692 intrusion and associated migmatites at a continental crust-mantle transition, Val
693 Malenco, Italy. *Schweizerische Mineral. und Petrogr. Mitteilungen* 81, 239–255.

694 Henk, A., Franz, L., Teufel, S., Oncken, O., 1997. Magmatic underplating, extension, and
695 crustal reequilibration: insights from a cross-section through the Ivrea Zone and Strona-
696 Ceneri Zone, Northern Italy. *J. Geol.* 105, 367–377.

697 Hermann, J., Müntener, O., 1996. Extension-related structures in the Malenco-Margna-
698 system: implications for paleogeography and consequences for rifting and Alpine
699 tectonics. *Schweizerische Mineral. und Petrogr. Mitteilungen* 76, 501–519.

700 Holyoke, C.W., Tullis, J., 2006. Mechanisms of weak phase interconnection and the effects of
701 phase strength contrast on fabric development. *J. Struct. Geol.* 28, 621–640.
702 doi:[10.1016/j.jsg.2006.01.008](https://doi.org/10.1016/j.jsg.2006.01.008)

703 Huismans, R.S., Beaumont, C., 2014. Rifted continental margins: The case for depth-
704 dependent extension. *Earth Planet. Sci. Lett.* 407, 148–162.
705 doi:<https://doi.org/10.1016/j.epsl.2014.09.032>

706 Jolivet, L., Gorini, C., Smit, J., Leroy, S., 2015. Continental breakup and the dynamics of
707 rifting in back-arc basins: The Gulf of Lion margin. *Tectonics* 34, 662–679.
708 doi:[10.1002/2014TC003570](https://doi.org/10.1002/2014TC003570)

709 Karner, G.D., Driscoll, N.W., Barker, D.H.N., 2003. Syn-rift regional subsidence across the
710 West African continental margin: the role of lower plate ductile extension. *Geol. Soc.
711 London, Spec. Publ.* 207, 105 LP-129.

712 Kenkmann, T., Dresen, G., 2002. Dislocation microstructure and phase distribution in a lower
713 crustal shear zone – an example from the Ivrea-Zone, Italy. *Int. J. Earth Sci.* 91, 445–
714 458. doi:[10.1007/s00531-001-0236-9](https://doi.org/10.1007/s00531-001-0236-9)

715 Kirby, S.H., 1983. Rheology of the lithosphere. *Rev. Geophys.* 21, 1458–1487.
716 doi:[10.1029/RG021i006p01458](https://doi.org/10.1029/RG021i006p01458)

717 Kuszniir, N.J., Karner, G.D., 2007. Continental lithospheric thinning and breakup in response
718 to upwelling divergent mantle flow: application to the Woodlark, Newfoundland and
719 Iberia margins. *Geol. Soc. London, Spec. Publ.* 282, 389 LP-419.

720 Langone, A., Padrón-Navarta José, A., Ji, W.-Q., Zanetti, A., Mazzucchelli, M., Tiepolo, M.,
721 Giovanardi, T., Bonazzi, M., 2017. Ductile–brittle deformation effects on crystal-
722 chemistry and U–Pb ages of magmatic and metasomatic zircons from a dyke of the
723 Finero Mafic Complex (Ivrea–Verbano Zone, Italian Alps). *Lithos* 284–285, 493–511.
724 doi:<https://doi.org/10.1016/j.lithos.2017.04.020>

725 Langone, A., Zanetti, A., Daczko, N.R., Piazzolo, S., Tiepolo, M., Mazzucchelli, M., 2018.
726 Zircon U–Pb dating of a lower crustal shear zone: a case study from the northern sector
727 of the Ivrea-Verbano Zone (Val Cannobina, Italy). *Tectonics* n/a-n/a.
728 doi:[10.1002/2017TC004638](https://doi.org/10.1002/2017TC004638)

729 Larsen, H.C., Mohn, G., Nirrengarten, M., Sun, Z., Stock, J., Jian, Z., Klaus, A., Alvarez-

- 730 Zarikian, C.A., Boaga, J., Bowden, S.A., Briais, A., Chen, Y., Cukur, D., Dadd, K.,
731 Ding, W., Dorais, M., Ferré, E.C., Ferreira, F., Furusawa, A., Gewecke, A., Hinojosa, J.,
732 Höfig, T.W., Hsiung, K.H., Huang, B., Huang, E., Huang, X.L., Jiang, S., Jin, H.,
733 Johnson, B.G., Kurzwski, R.M., Lei, C., Li, B., Li, L., Li, Y., Lin, J., Liu, C., Liu, C.,
734 Liu, Z., Luna, A.J., Lupi, C., McCarthy, A., Ningthoujam, L., Osono, N., Peate, D.W.,
735 Persaud, P., Qiu, N., Robinson, C., Satolli, S., Sauermilch, I., Schindlbeck, J.C., Skinner,
736 S., Straub, S., Su, X., Su, C., Tian, L., van der Zwan, F.M., Wan, S., Wu, H., Xiang, R.,
737 Yadav, R., Yi, L., Yu, P.S., Zhang, C., Zhang, J., Zhang, Y., Zhao, N., Zhong, G.,
738 Zhong, L., 2018. Rapid transition from continental breakup to igneous oceanic crust in
739 the South China Sea. *Nat. Geosci.* 11, 782–789. doi:10.1038/s41561-018-0198-1
- 740 Mackwell, S.J., Zimmerman, M.E., Kohlstedt, D.L., 1998. High- temperature deformation of
741 dry diabase with application to tectonics on Venus. *J. Geophys. Res. Solid Earth* 103,
742 975–984. doi:10.1029/97JB02671
- 743 Manatschal, G., Lavier, L., Chenin, P., 2015. The role of inheritance in structuring
744 hyperextended rift systems: Some considerations based on observations and numerical
745 modeling. *Gondwana Res.* 27, 140–164. doi:http://dx.doi.org/10.1016/j.gr.2014.08.006
- 746 Manatschal, G., Nievergelt, P., 1997. A continent-ocean transition recorded in the Err and
747 Platta nappes (Eastern Switzerland). *Eclogae Geol. Helv.* 90, 3–27.
- 748 Masini, E., Manatschal, G., Mohn, G., Ghienne, J.-F., Lafont, F., 2011. The tectono-
749 sedimentary evolution of a supra-detachment rift basin at a deep-water magma-poor
750 rifted margin: the example of the Samedan Basin preserved in the Err nappe in SE
751 Switzerland. *Basin Res.* 23, 652–677. doi:10.1111/j.1365-2117.2011.00509.x
- 752 Mohn, G., Manatschal, G., Beltrando, M., Masini, E., Kuszniir, N., 2012. Necking of
753 continental crust in magma-poor rifted margins: Evidence from the fossil Alpine Tethys
754 margins. *Tectonics* 31, 1–28.
- 755 Mohn, G., Manatschal, G., Masini, E., Müntener, O., 2011. Rift-related inheritance in
756 orogens: a case study from the Austroalpine nappes in Central Alps (SE-Switzerland and
757 N-Italy). *Int. J. Earth Sci.* 100, 937–961. doi:10.1007/s00531-010-0630-2
- 758 Mohn, G., Manatschal, G., Müntener, O., Beltrando, M., Masini, E., 2010. Unravelling the
759 interaction between tectonic and sedimentary processes during lithospheric thinning in
760 the Alpine Tethys margins. *Int. J. Earth Sci.* 99, 75–101. doi:10.1007/s00531-010-0566-
761 6
- 762 Mulch, A., Cosca, M., Handy, M., 2002a. In-situ UV-laser $^{40}\text{Ar}/^{39}\text{Ar}$ geochronology of a
763 micaceous mylonite: an example of defect-enhanced argon loss. *Contrib. to Mineral.
764 Petrol.* 142, 738–752. doi:10.1007/s00410-001-0325-6
- 765 Mulch, A., Rosenau, M., Dörr, W., Handy, M., 2002b. The age and structure of dikes along
766 the tectonic contact of the Ivrea-Verbano and Strona-Ceneri Zones (southern Alps,
767 Northern Italy, Switzerland). *Schweizerische Mineral. und Petrogr. Mitteilungen* 82, 55–
768 76.
- 769 Müntener, O., Hermann, J., 2001. The role of lower crust and continental upper mantle during
770 formation of non-volcanic passive margins: evidence from the Alps. *Geol. Soc. London,
771 Spec. Publ.* 187, 267–288. doi:10.1144/gsl.sp.2001.187.01.13
- 772 Müntener, O., Hermann, J., Trommsdorff, V., 2000. Cooling History and Exhumation of
773 Lower-Crustal Granulite and Upper Mantle (Malenco, Eastern Central Alps). *J. Petrol.*
774 41, 175–200. doi:10.1093/petrology/41.2.175
- 775 Müntener, O., Manatschal, G., Desmurs, L., Pettke, T., 2010. Plagioclase Peridotites in
776 Ocean–Continent Transitions: Refertilized Mantle Domains Generated by Melt
777 Stagnation in the Shallow Mantle Lithosphere. *J. Petrol.* 51, 255–294.
778 doi:10.1093/petrology/egp087
- 779 Osmundsen, P.T., Ebbing, J., 2008. Styles of extension offshore mid-Norway and

780 implications for mechanisms of crustal thinning at passive margins. *Tectonics* 27, 1–25.
781 doi:10.1029/2007TC002242

782 Péron-Pinvidic, G., Manatschal, G., 2009. The final rifting evolution at deep magma-poor
783 passive margins from Iberia-Newfoundland: a new point of view. *Int. J. Earth Sci.* 98,
784 1581–1597. doi:10.1007/s00531-008-0337-9

785 Petri, B., Mohn, G., Skrzypek, E., Mateeva, T., Galster, F., Manatschal, G., 2017. U–Pb
786 geochronology of the Sondalo gabbroic complex (Central Alps) and its position within
787 the Permian post-Variscan extension. *Int. J. Earth Sci.* 106, 2873–2893.
788 doi:10.1007/s00531-017-1465-x

789 Petri, B., Mohn, G., Štípská, P., Schulmann, K., Manatschal, G., 2016. The Sondalo gabbro
790 contact aureole (Campo unit, Eastern Alps): implications for mid-crustal mafic magma
791 emplacement. *Contrib. to Mineral. Petrol.* 171, 52. doi:10.1007/s00410-016-1263-7

792 Petri, B., Skrzypek, E., Mohn, G., Mateeva, T., Robion, P., Schulmann, K., Manatschal, G.,
793 Müntener, O., 2018. Mechanical anisotropies and mechanisms of mafic magma ascent in
794 the middle continental crust: The Sondalo magmatic system (N Italy). *GSA Bull.* 130,
795 331–352. doi:10.1130/B31693.1

796 Popov, A.A., Sobolev, S. V., 2008. SLIM3D: A tool for three-dimensional thermomechanical
797 modeling of lithospheric deformation with elasto-visco-plastic rheology. *Phys. Earth
798 Planet. Inter.* 171, 55–75. doi:https://doi.org/10.1016/j.pepi.2008.03.007

799 Quick, J.E., Sinigoi, S., Snoke, A.W., Kalakay, T.J., Mayer, A., Peressini, G., 2003. Geologic
800 map of the southern Ivrea-Verbano Zone, northwestern Italy: U.S. Geological Survey
801 Geologic Investigations Series Map I-2776, scale 1:25,000 22 p.

802 Rader, E., Emry, E., Schmerr, N., Frost, D., Cheng, C., Menard, J., Yu, C.-Q., Geist, D., 2015.
803 Characterization and Petrological Constraints of the Midlithospheric Discontinuity.
804 *Geochemistry, Geophys. Geosystems* 16, 3484–3504. doi:10.1002/2015GC005943

805 Reston, T., 2007a. Extension discrepancy at North Atlantic nonvolcanic rifted margins:
806 Depth-dependent stretching or unrecognized faulting? *Geology* 35, 367–370.

807 Reston, T., 2007b. The formation of non-volcanic rifted margins by the progressive extension
808 of the lithosphere: the example of the West Iberian margin. *Geol. Soc. London, Spec.
809 Publ.* 282, 77 LP-110.

810 Reston, T.J., 1988. Evidence for shear zones in the lower crust offshore Britain. *Tectonics* 7,
811 929–945. doi:10.1029/TC007i005p00929

812 Reston, T.J., Krawczyk, C.M., Klaeschen, D., 1996. The S reflector west of Galicia (Spain):
813 Evidence from prestack depth migration for detachment faulting during continental
814 breakup. *J. Geophys. Res. Solid Earth* 101, 8075–8091. doi:10.1029/95JB03466

815 Ros, E., Pérez-Gussinyé, M., Araújo, M., Thoaldo Romeiro, M., Andrés-Martínez, M.,
816 Morgan, J.P., 2017. Lower Crustal Strength Controls on Melting and Serpentinization at
817 Magma-Poor Margins: Potential Implications for the South Atlantic. *Geochemistry,
818 Geophys. Geosystems* 18, 4538–4557. doi:10.1002/2017GC007212

819 Rybacki, E., Dresen, G., 2004. Deformation mechanism maps for feldspar rocks.
820 *Tectonophysics* 382, 173–187. doi:https://doi.org/10.1016/j.tecto.2004.01.006

821 Schmalholz, S.M., Duretz, T., 2017. Impact of grain size evolution on necking in calcite
822 layers deforming by combined diffusion and dislocation creep. *J. Struct. Geol.* 103, 37–
823 56. doi:https://doi.org/10.1016/j.jsg.2017.08.007

824 Schmalholz, S.M., Mancktelow, N.S., 2016. Folding and necking across the scales: a review
825 of theoretical and experimental results and their applications. *Solid Earth* 7, 1417–1465.
826 doi:10.5194/se-7-1417-2016

827 Schmid, S.M., Zingg, A., Handy, M., 1987. The kinematics of movements along the Insubric
828 Line and the emplacement of the Ivrea Zone. *Tectonophysics* 135, 47–66.
829 doi:http://dx.doi.org/10.1016/0040-1951(87)90151-X

830 Schuster, R., Stüwe, K., 2008. Permian metamorphic event in the Alps. *Geology* 36, 603–606.
831 doi:10.1130/G24703A.1

832 Shea, W.T., Kronenberg, A.K., 1993. Strength and anisotropy of foliated rocks with varied
833 mica contents. *J. Struct. Geol.* 15, 1097–1121. doi:https://doi.org/10.1016/0191-
834 8141(93)90158-7

835 Siegesmund, S., Layer, P., Dunkl, I., Vollbrecht, A., Steenken, A., Wemmer, K., Ahrendt, H.,
836 2008. Exhumation and deformation history of the lower crustal section of the Valstrona
837 di Omegna in the Ivrea Zone, southern Alps. *Geol. Soc. London, Spec. Publ.* 298, 45–68.
838 doi:10.1144/sp298.3

839 Spalla, M.I., Zandoni, D., Marotta, A.M., Rebay, G., Roda, M., Zucali, M., Gosso, G., 2014.
840 The transition from Variscan collision to continental break-up in the Alps: insights from
841 the comparison between natural data and numerical model predictions. *Geol. Soc.*
842 *London, Spec. Publ.* 405. doi:10.1144/sp405.11

843 Thybo, H., Artemieva, I.M., 2013. Moho and magmatic underplating in continental
844 lithosphere. *Tectonophysics* 609, 605–619.
845 doi:http://dx.doi.org/10.1016/j.tecto.2013.05.032

846 Tugend, J., Gillard, M., Manatschal, G., Nirrengarten, M., Harkin, C., Epin, M.-E., Sauter, D.,
847 Autin, J., Kusznir, N., McDermott, K., 2018. Reappraisal of the magma-rich versus
848 magma-poor rifted margin archetypes. *Geol. Soc. London, Spec. Publ.* 476, SP476.9.
849 doi:10.1144/SP476.9

850 Tommasi, A., Vauchez, A., 2001. Continental rifting parallel to ancient collisional belts: an
851 effect of the mechanical anisotropy of the lithospheric mantle. *Earth Planet. Sci. Lett.*
852 185, 199–210. doi:https://doi.org/10.1016/S0012-821X(00)00350-2

853 Von Quadt, A., Grünenfelder, M., Büchi, H., 1994. U-Pb zircon ages from igneous rocks of
854 the Bernina nappe system (Grisons, Switzerland). *Schweizerische Mineral. und Petrogr.*
855 *Mitteilungen* 74, 373–382.

856 von Raumer, J.F., Bussy, F., Schaltegger, U., Schulz, B., Stampfli, G.M., 2013. Pre-Mesozoic
857 Alpine basements—Their place in the European Paleozoic framework. *Geol. Soc. Am.*
858 *Bull.* 125, 89–108.

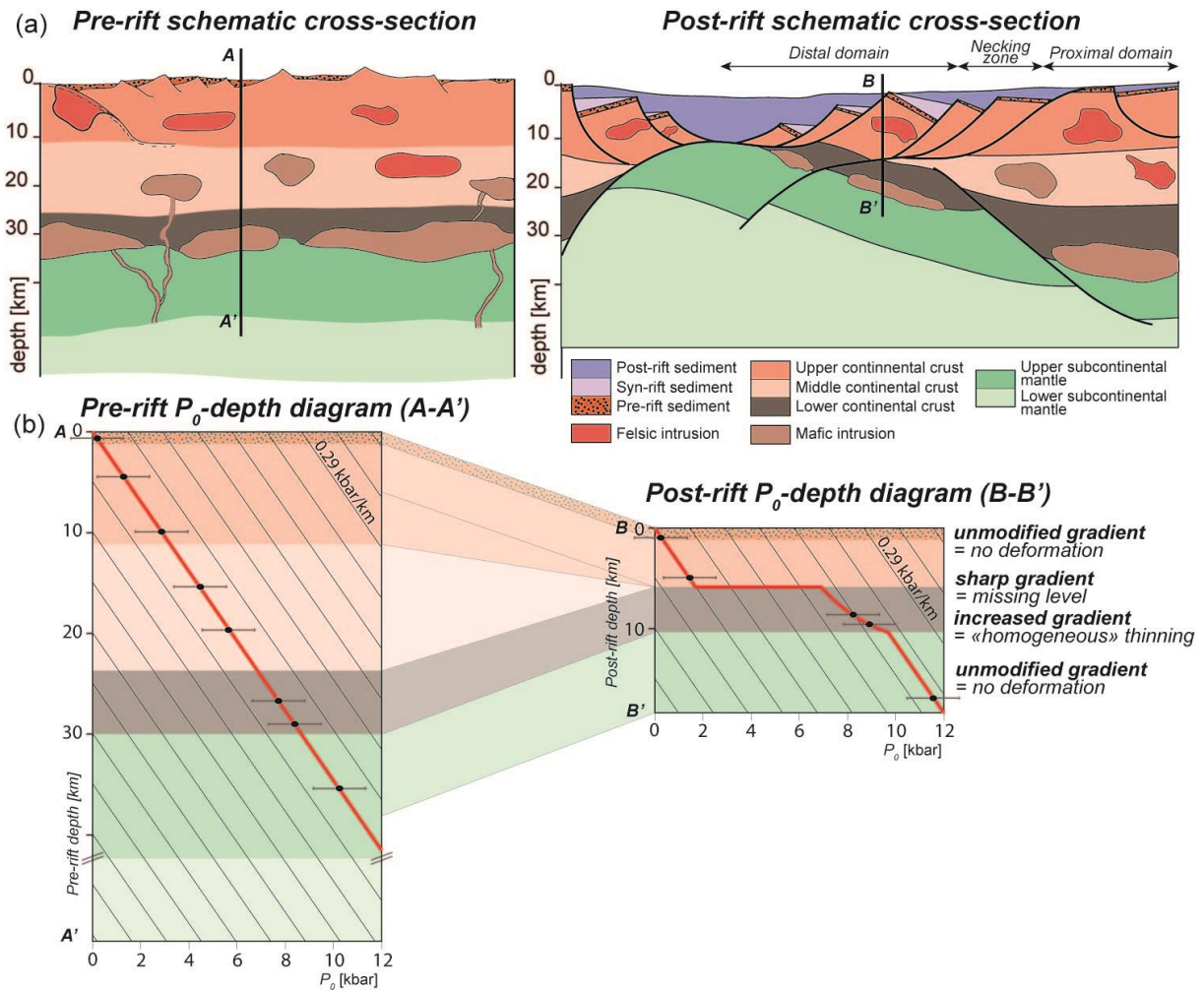
859 Whitmarsh, R.B., Dean, S.M., Minshull, T.A., Tompkins, M., 2000. Tectonic implications of
860 exposure of lower continental crust beneath the Iberia Abyssal Plain, Northeast Atlantic
861 Ocean: Geophysical evidence. *Tectonics* 19, 919–942. doi:10.1029/2000TC900016

862 Wintsch, R.P., Christoffersen, R., Kronenberg, A.K., 1995. Fluid-rock reaction weakening of
863 fault zones. *J. Geophys. Res. Solid Earth* 100, 13021–13032. doi:10.1029/94JB02622

864 Wolff, R., Dunkl, I., Kiesselbach, G., Wemmer, K., Siegesmund, S., 2012.
865 Thermochronological constraints on the multiphase exhumation history of the Ivrea-
866 Verbano Zone of the Southern Alps. *Tectonophysics* 579, 104–117.
867 doi:http://dx.doi.org/10.1016/j.tecto.2012.03.019

868 Zastrozhnov, D., Gernigon, L., Gogin, I., Abdelmalak, M.M., Planke, S., Faleide, J.I., Eide,
869 S., Myklebust, R., 2018. Cretaceous-Paleocene Evolution and Crustal Structure of the
870 Northern Vøring Margin (Offshore Mid-Norway): Results from Integrated Geological
871 and Geophysical Study. *Tectonics*. doi:10.1002/2017TC004655

872 Zingg, A., Handy, M.R., Hunziker, J.C., Schmid, S.M., 1990. Tectonometamorphic history of
873 the Ivrea Zone and its relationship to the crustal evolution of the Southern Alps.
874 *Tectonophysics* 182, 169–192. doi:http://dx.doi.org/10.1016/0040-1951(90)90349-D
875



877

878

879

880

881

882

883

884

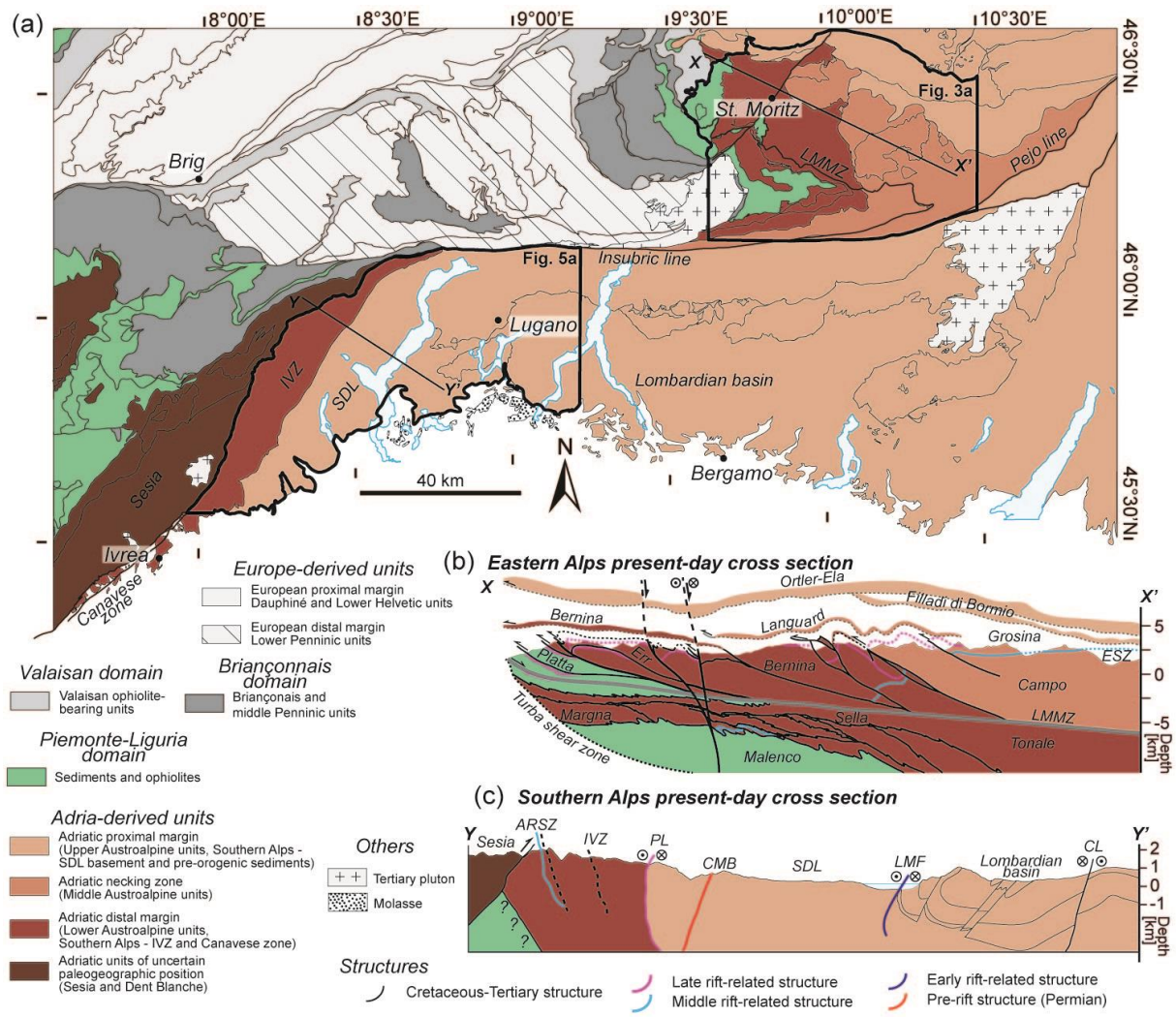
885

886

887

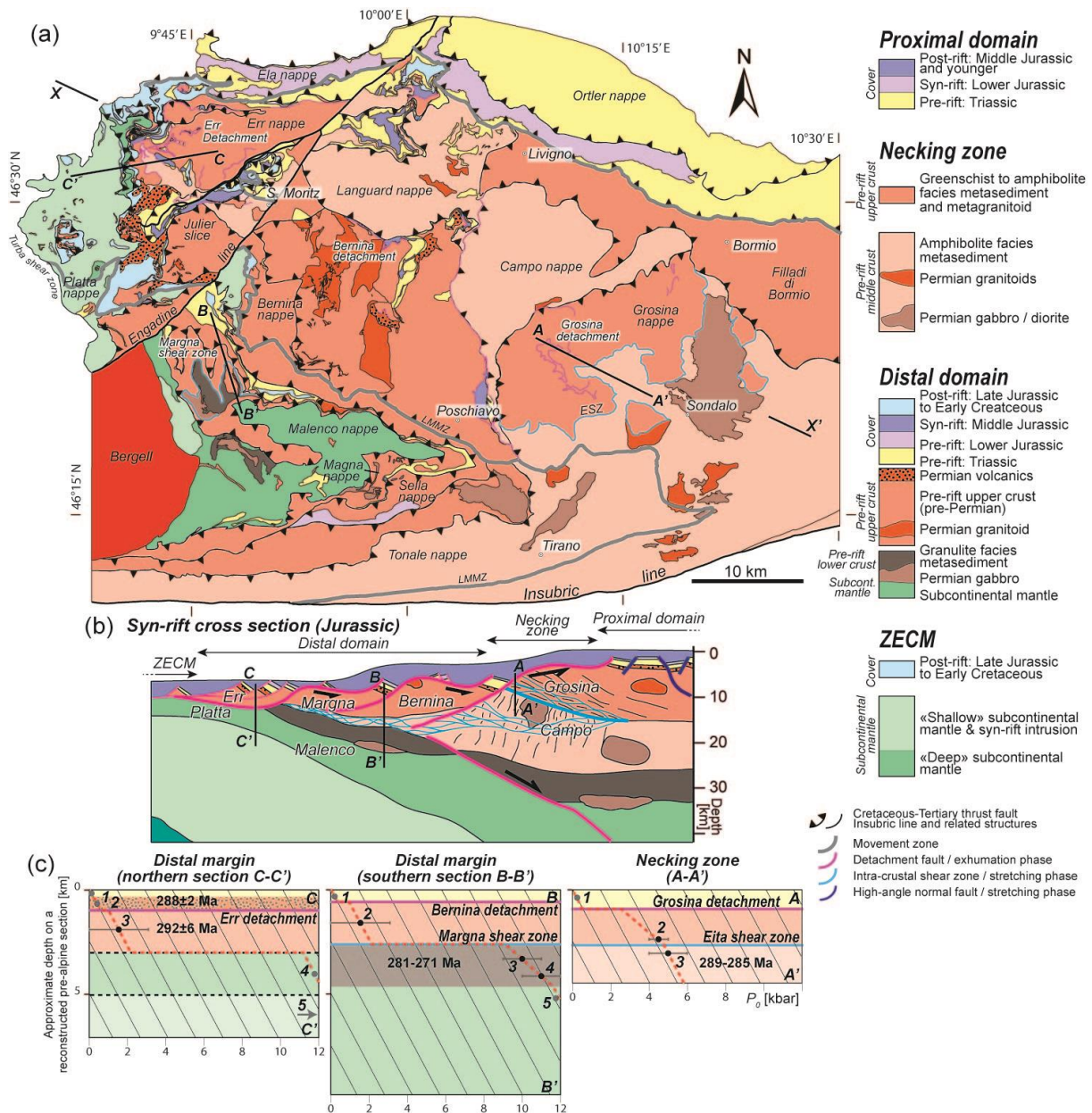
Fig. 1: (a) Pre-rift and post-rift schematic sections. Pre-rift section (modified from Mohn et al., 2010; Petri et al., 2017) illustrates the architecture of the pre-rift continental lithosphere with mafic plutons in the lower crust, mafic and felsic plutons in the middle crust and felsic plutons in the upper crust. Post-rift section (modified from Mohn et al., 2012) illustrates the general lithospheric architecture of hyper-extended rift basin. (b) Synthetic P_0 -depth diagrams elaborated along a pre-rift section (A-A') and along the distal domain of a post-rift section (B-B'). The gradient is linear along the pre-rift section A-A' while different patterns are seen in post-rift section B-B': (1) unmodified gradient compared to pre-rift section in portions that escaped rift-related deformation, (2) sharp gradient in places where pre-rift crustal or lithospheric levels are missing, and (3) increased gradients when rift-related

888 deformation is “homogeneously” distributed across a unit. $0.29 \text{ kbar.km}^{-1}$ is chosen as a
 889 reasonable maximum lithostatic pressure gradient (see text).



890

891 **Fig. 2:** (a) Tectonic map of the Southern and Central Alps compiled from the Swiss
 892 and Italian geological maps and from Müntener and Hermann (2001). (b,c) Present-day
 893 schematic cross sections across (b) the Eastern Alps (location also on Fig. 3; modified from
 894 Mohn et al., 2011) and (c) the Southern Alps (location also on Fig. 5; modified from Zingg et
 895 al., 1990). ARSZ: Anzola-Rosarolo Shear Zone; CL: Cremossina line; CMB: Cossato-
 896 Mergozzo-Brissago Line; FSZ: Finero Shear Zones; IVZ; Ivrea-Verbano Zone; LMF: Lago
 897 Maggiore Fault; LVG: Lugano Val Grande Fault; LMMZ: Lunghin-Mortirolo Movement
 898 Zone; PL: Pogallo Line; SDL: Serie Dei Laghi.



899

900 **Fig. 3:** Lithotectonic map of Austroalpine and Upper Penninic units in SE Switzerland

901 and N Italy. (b) Reconstructed post-rift section modified from Mohn et al. (2012). (c)

902 Schematic P_0 -depth diagrams built using field observations, and P - T estimates (see text and

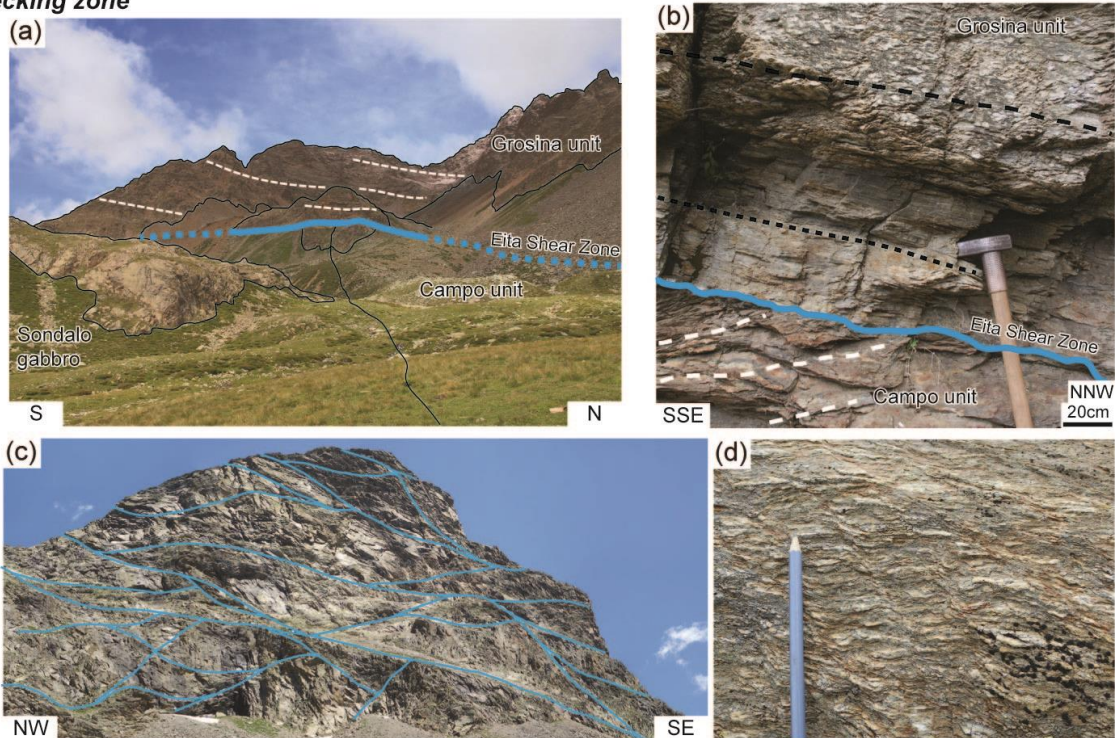
903 Table S1 for references). Schematic P_0 -depth diagrams are shown for the necking zone (A-

904 A'), the southern distal section (B-B'), for the northern distal section (C-C'). Due to Alpine

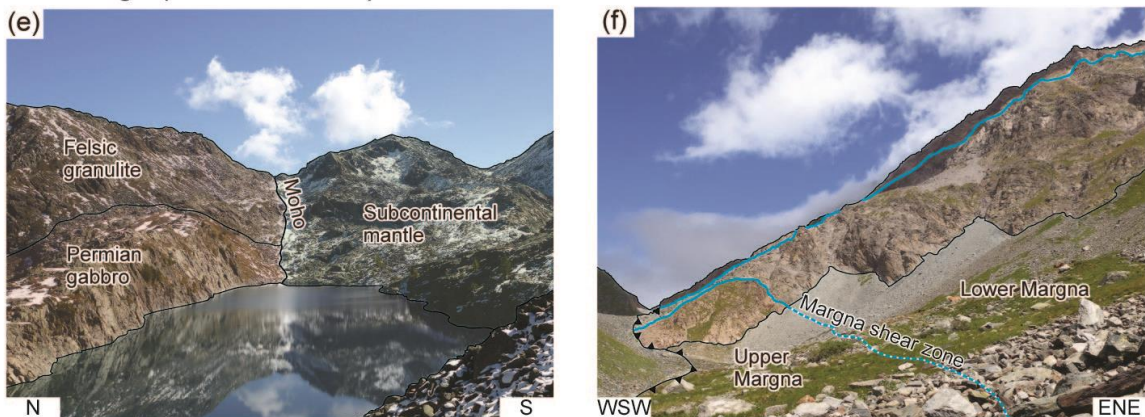
905 deformation, unit thickness is only estimated. ESZ: Eita Shear Zone; LMMZ: Lunghin-

906 Mortirolo Movement Zone. Location of X-X' section on Fig. 2.

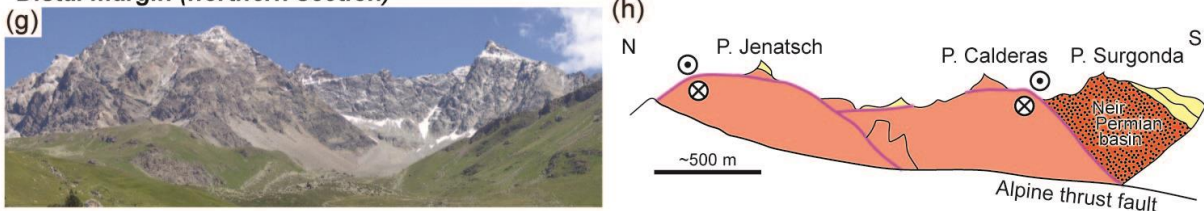
Necking zone



Distal margin (southern section)



Distal margin (northern section)



907

908

909

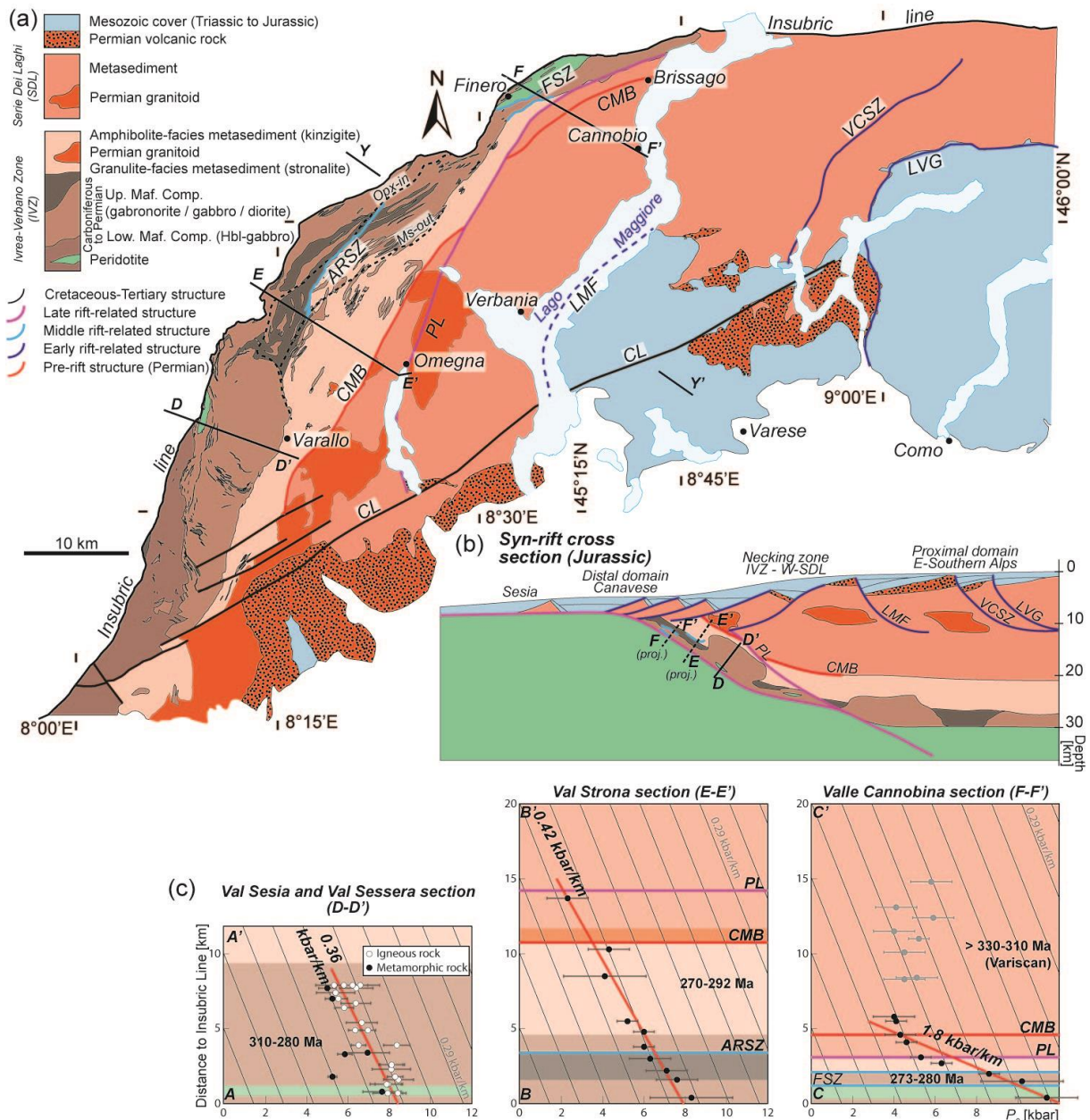
910

911

912

Fig. 4: Field photographs from the Eastern Alps. Necking zone: (a) panoramic view on the Jurassic Eita Shear Zone (ESZ) marking the contact between the Grosina unit and the Campo unit intruded by the Permian Sondalo gabbro. (b) Contact between the Campo and Grosina units delimited by the Eita shear zone. (c) Anastomosing extensional shear zones distributed across the entire Grosina unit. In contrast, the Campo unit is devoid of such

913 extensional structures. (d) Zoom of S-C structures in one of the anastomosing shear zones
914 from the Grosina unit. Southern distal margin: (e) lower crust / upper mantle contact
915 preserved in the Malenco unit. The pre-rift lower crust is characterized by the emplacement of
916 the Permian Braccia gabbro; (f) the Margna shear zone in the hinge of an Alpine recumbent
917 fold. This structure delimits the pre-rift upper crust (Upper Margna - Fora gneiss) from the
918 pre-rift lower crust (Lower Margna - Feddoz gabbro). Northern distal margin: (g-h)
919 panoramic view and interpreted N-S section on the Err unit and the Neir Permian basin. The
920 geometry and localization of the Jurassic Err and Jenatsch detachment faults are at least partly
921 controlled by the pre-rift Neir Permian basin (modified from Manatschal et al., 2015).



922

923

Fig. 5: (a) Lithotectonic map of the Southern Alps modified from Handy *et al.* (1999),

924

Quick *et al.* (2003), Beltrando *et al.* (2015b) and the 1:200,000 geological maps from Italy

925

and Switzerland. (b) Reconstructed post-rift cross-section modified from Beltrando *et al.*

926

(2015b). (c) P_0 -depth diagrams for the Val Sessera – Val Sesia section (D-D'), the Val Strona

927

section (E-E') and the Valle Cannobina section (F-F'). The diagrams are here plotted as P_0 -

928

distance to the Insubric line as the pre-rift IVZ is tilted to 90°, with almost no Alpine

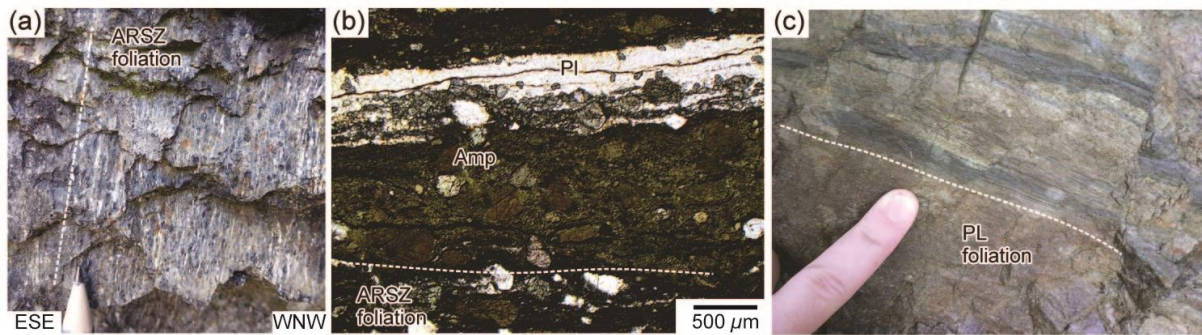
929

deformation. See text and Table S2 for references. ARSZ: Anzola-Rosarolo Shear Zone; CL:

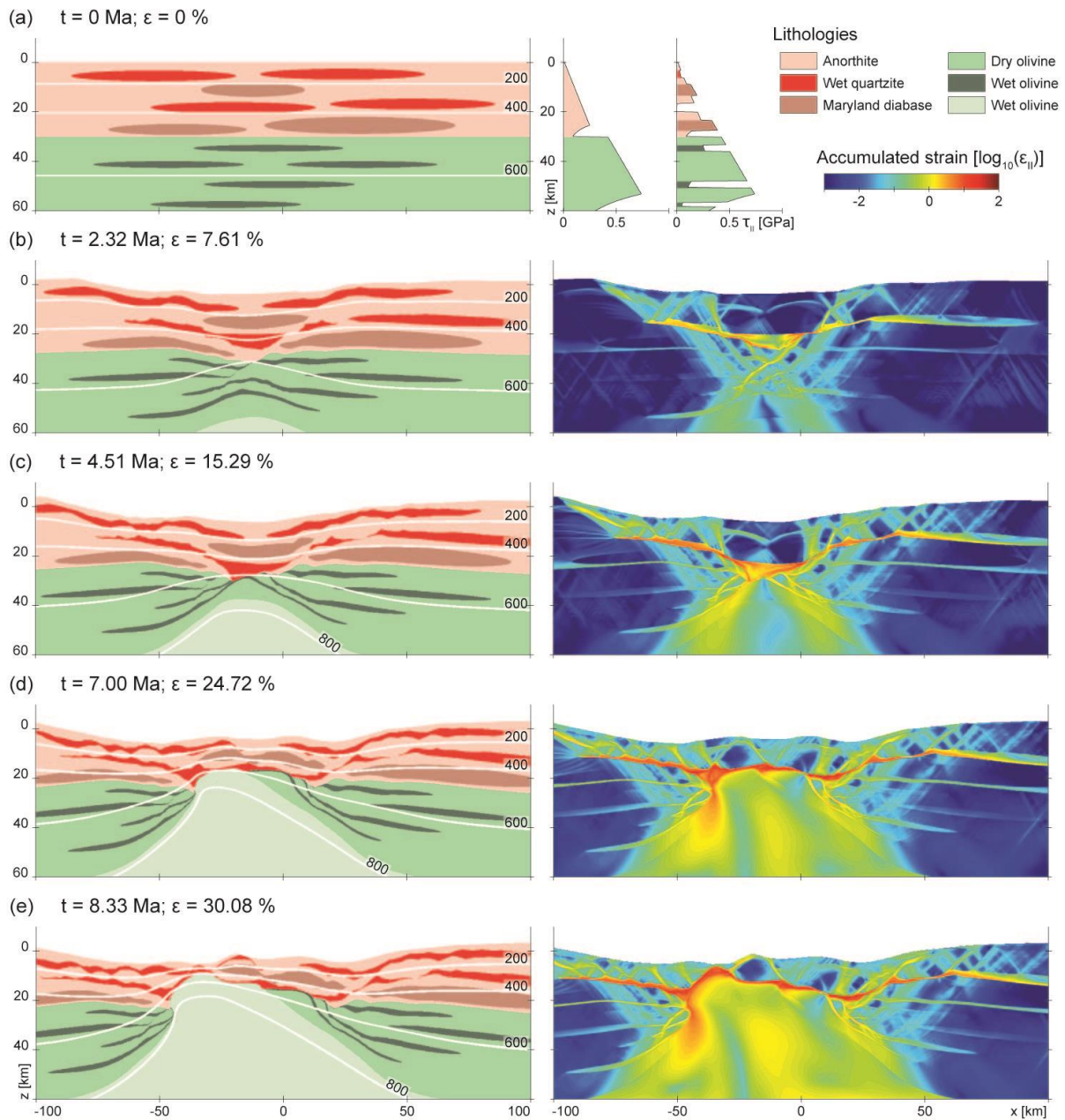
930

Cremossina Line; CMB: Cossato-Mergozo-Brissago Line; FSZ: Finero Shear Zones; LMF:

931 Lago Maggiore Fault; LVG: Lugano Val Grande Fault; PL: Pogallo Line; VCSZ: Val Cola
932 Shear Zone. Location of Y-Y' section on Fig. 2.



933
934 Fig. 6: Field photographs and microphotograph from the Southern Alps. (a,b) the
935 Anzola-Rosarolo Shear Zone (ARSZ) showing dynamic recrystallization of plagioclase,
936 amphibole and pyroxene. (c) The Pogallo line showing greenschist facies deformation.



937

938

939

940

941

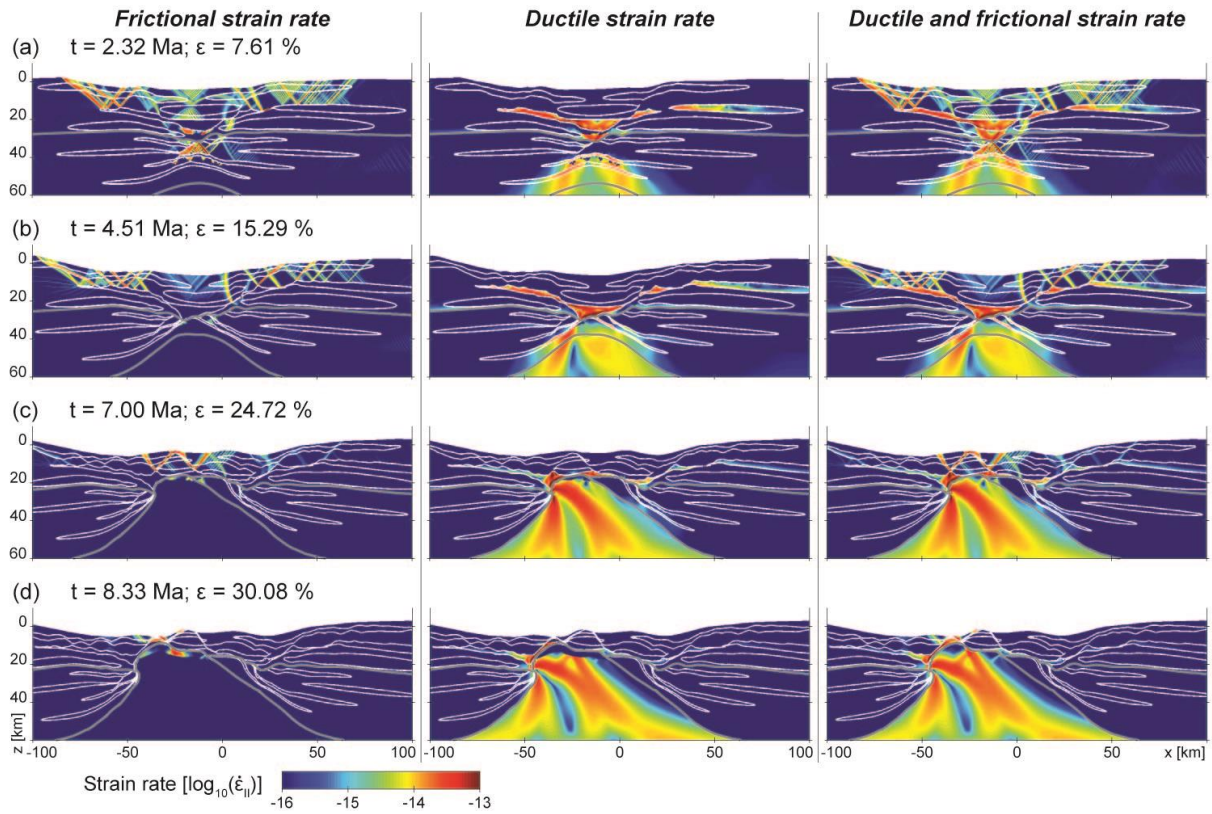
942

943

944

945

Fig. 7: Initial configuration and evolution of the reference numerical model. (a) Initial distribution of the compositional field (enlargement, left column) and initial strength profiles (right column) corresponding to a homogeneous strength profile of the lithosphere (i.e. crossing no initial heterogeneities, leftmost) and heterogeneous strength profile ($x = 0$ km) of the lithosphere (i.e. crossing initial heterogeneities, rightmost). Panels (b) to (e) depict the evolution of the reference model both in terms of compositional, thermal fields (left column) and accumulated strain (right column). White lines denote isotherms with 200 °C spacing. The accumulated strain was reported for the corresponding amounts of extension.



946

947

Fig. 8: Partitioning of the strain rate between the frictional (Drucker-Prager rheology)

948

and ductile rheology (viscous creep). Panels (a) to (d) correspond to a progressive time

949

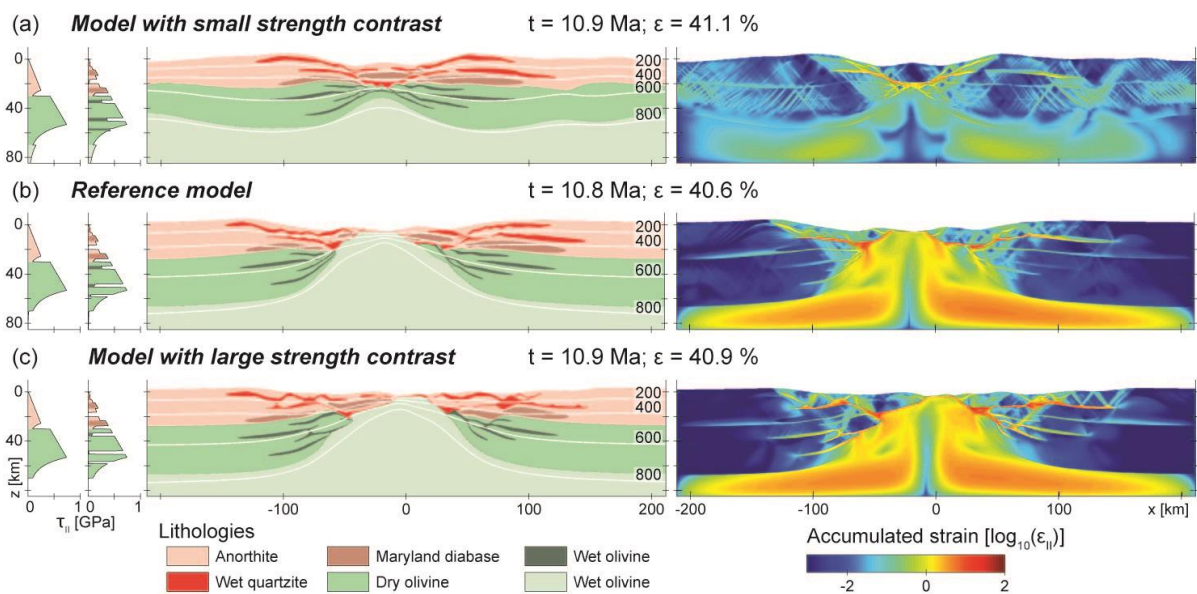
evolution. The white lines correspond to the contours of heterogeneities and the grey lines

950

correspond to the Moho and the base of upper subcontinental mantle highlighting the evolving

951

morphology of the main contacts and heterogeneities.



952

953 Fig. 9: Influence of the rheological contrasts on the style of lithospheric extension.

954 Panel (a) corresponds to a model with reduced strength contrast compared to the reference

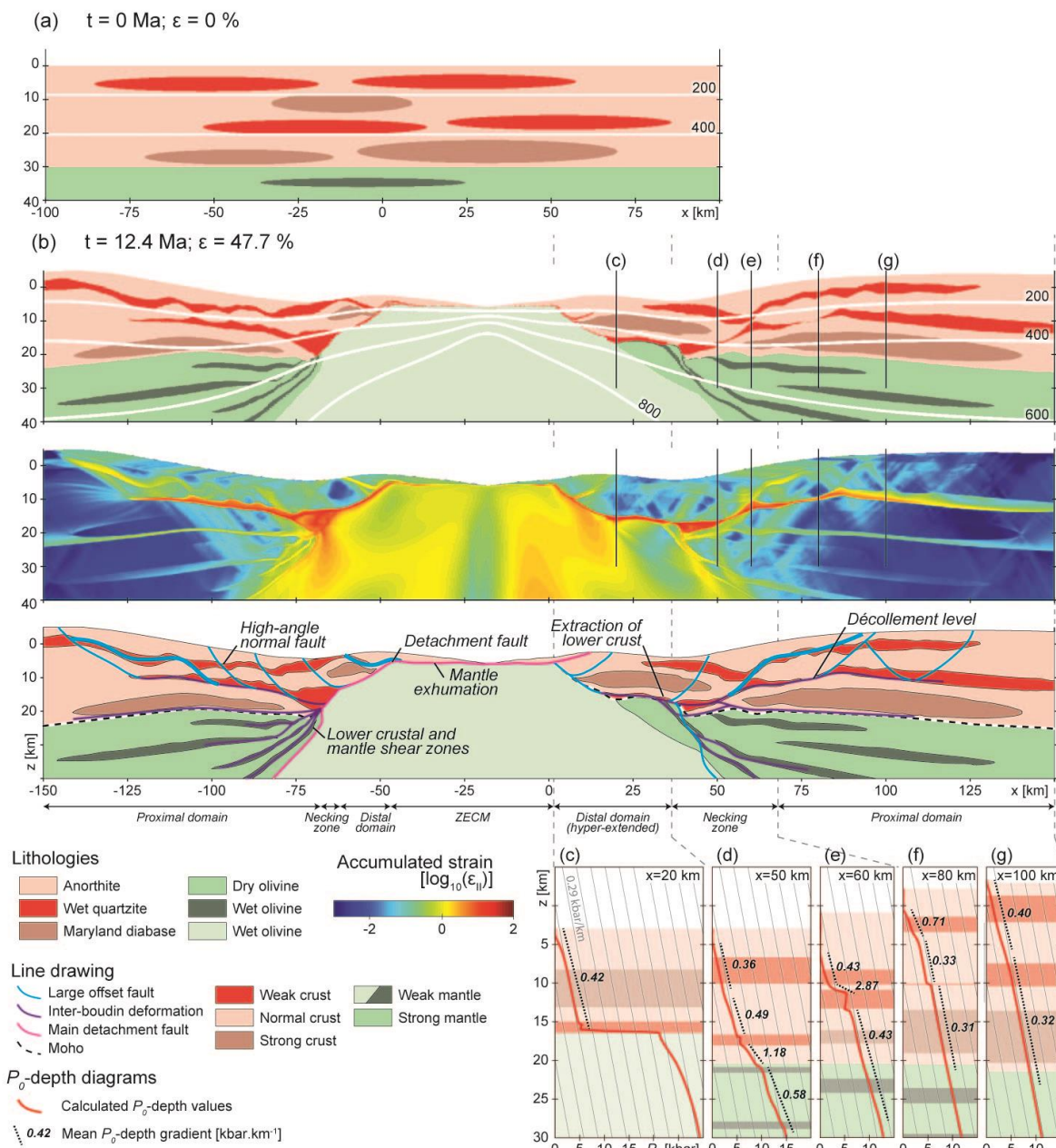
955 model (see text). Panel (b) depicts the reference model. Panel (c) corresponds to a model with

956 enlarged strength contrasts compared to the reference model. For each panel, we report initial

957 strength profiles corresponding to lithosphere portions including heterogeneities or not (left),

958 compositional and thermal field (isotherms depicted for each 200 °C), and the accumulated

959 strain pattern.



960

961 Fig. 10: (a) Pre-rift architecture of the continental lithosphere with the localization of
962 the heterogeneities. (b) Post-rift margin architecture showing from the top to bottom:
963 compositional and thermal fields (200 °C spacing), accumulated strain and line drawing
964 highlighting the different recognized structures. Modeled P_θ -depth diagrams and calculated
965 gradients across (c) the distal domain, (d,e) the necking zone and (f,g) the proximal domain.
966 ZECM: Zone of Exhumed Continental Mantle.